

**Necroplanetology:  
Disrupted Planetary Material  
Transiting WD1145+017**

by

Girish Duvvuri  
Class of 2017

A thesis submitted to the  
faculty of Wesleyan University  
in partial fulfillment of the requirements for the  
Degree of Bachelor of Arts  
with Departmental Honors in Astronomy

---

*When we say “the world has ended,” it’s usually a lie, because the planet is just fine. But this is the way the world ends.*

–N.K. JEMISIN

*The Fifth Season*

---

# Acknowledgements

This project would not have been possible without the guidance and mentorship of my advisor Seth Redfield. His enthusiasm for my work and belief in my capacity to do it frequently exceeded my own and I am grateful for the privilege of working with and learning from him.

I would also like to thank the Wesleyan Astronomy department as a whole for welcoming me to a better community than I could have ever imagined before coming here. In particular, I would like to thank my fellow basement dwellers and friends—Julian, Simon, Rachel and Zach—for their part in making the ridiculously long hours we spent in the observatory enjoyable. Between `slither.io` and Medical Mondays, we may not have always been particularly productive.

Roxie and Sarah both indulged my rambling and general misanthropy for the past few years and their intensification in the last two semesters. Lyn and Luna's hospitality and gentle suggestions to leave both basements every now and then helped keep me sane(-ish). They helped remind me that I have a life.

I thank Wesleyan University for computer time supported by the NSF under grant number CNS-0619508 and the Wesleyan Summer Research in the Sciences program for supporting my research. This work includes data collected by the K2 mission. K2 Cycle 1 funding provided support for this work through NASA grant NNX15AV84G. Funding for the K2 mission is provided by the NASA Science Mission directorate.

Finally, I would like thank my brother for his role in my life. I hope that one day you read this and show me a project of your own.

# Contents

|          |  |           |
|----------|--|-----------|
| <b>1</b> | <b>Introduction</b>                                | <b>1</b>  |
| 1.1      | White Dwarf Planetary Systems . . . . .            | 1         |
| 1.2      | White Dwarf Transits . . . . .                     | 3         |
| 1.3      | Detection of Transits of WD1145+017 . . . . .      | 5         |
| <b>2</b> | <b>Spectroscopy</b>                                | <b>9</b>  |
| 2.1      | Datasets . . . . .                                 | 10        |
| 2.1.1    | <i>Keck / HIRES</i> . . . . .                      | 10        |
| 2.1.2    | <i>VLT / X-Shooter</i> . . . . .                   | 10        |
| 2.2      | Fitting Circumstellar Absorption (CSA) . . . . .   | 11        |
| 2.2.1    | Finding CSA Lines . . . . .                        | 11        |
| 2.2.2    | Characterizing CSA Features . . . . .              | 14        |
| 2.3      | CSA Variability . . . . .                          | 18        |
| 2.4      | Disk Modeling . . . . .                            | 24        |
| <b>3</b> | <b>Stability</b>                                   | <b>25</b> |
| 3.1      | Constraints on Mass, Eccentricity, $N_f$ . . . . . | 25        |
| 3.1.1    | Simulation Parameters . . . . .                    | 26        |
| 3.1.2    | Characterizing Instability . . . . .               | 29        |
| 3.2      | Implications for WD1145+017 . . . . .              | 31        |

|          |   |           |
|----------|---|-----------|
| <b>4</b> | <b>Disruption</b>   | <b>36</b> |
| 4.1      | Rubble Piles . . . . .  | 36        |
| 4.1.1    | Hexagonal and Random Packing . . . . .                            | 37        |
| 4.1.2    | Force-Biased Algorithm . . . . .                                  | 39        |
| 4.1.3    | Rubble Pile Parameters . . . . .                                  | 40        |
| 4.2      | REBOUND and PKDGRAV Discrepancies . . . . .                       | 43        |
| 4.3      | Debris Cloud Approximation . . . . .                              | 45        |
| 4.3.1    | Known and Inferred Properties of the Planetary Material . . . . . | 47        |
| 4.3.2    | Simulation Parameters . . . . .                                   | 49        |
| 4.3.3    | Savitzky-Golay Filtering . . . . .                                | 50        |
| 4.3.4    | Effects of Structure on Template Lightcurves . . . . .            | 50        |
| <b>5</b> | <b>Photometry</b>   | <b>55</b> |
| 5.1      | Summary of Features from all Datasets . . . . .                   | 55        |
| 5.2      | Fitting with Templates . . . . .                                  | 59        |
| 5.3      | “Forward Modelling” . . . . .                                     | 64        |
| <b>6</b> | <b>Conclusions and Future Work</b>                                | <b>66</b> |
| 6.1      | Possible Formation/Destruction Scenario . . . . .                 | 67        |
| 6.2      | Future Work . . . . .   | 68        |
| <b>A</b> | <b>REBOUND N-body Code</b>  | <b>69</b> |
| A.1      | Background . . . . .  | 69        |
| A.2      | Integrators . . . . .   | 69        |
| A.2.1    | Drift-Kick-Drift . . . . .  | 70        |
| A.2.2    | Leapfrog Integrator . . . . .                                     | 71        |
| A.2.3    | WHFAST . . . . .  | 71        |

|       |                     |           |
|-------|---------------------|-----------|
| A.2.4 | IAS15 . . . . .     | 74        |
| A.2.5 | HERMES . . . . .    | 76        |
|       | <b>Bibliography</b> | <b>78</b> |

# Chapter 1

## Introduction

The knowledge that our planet was one of many in the Solar System inevitably leads to the question of what the others are like, and as with most scientific endeavors every question answered raises an entirely new set. But until relatively recently, we were limited to the small sample of planets orbiting our Sun. Speculation about the presence and/or nature of “extrasolar” planets, or exoplanets, remained just that: speculative. Then Wolszczan & Frail (1992) showed that variations in a pulsar’s rotational period were consistent with the orbits of two Earth-mass objects. A few years later, observations of the radial motion of 51 Peg b (Mayor & Queloz 1995) demonstrated the presence of a Jupiter-mass planet orbiting a Sun-like star with a period of 4.23 days, something entirely alien to our Solar System and models of planet formation. Later surveys with this radial velocity (RV, see Figure 1.1) method expanded our sample of exoplanets, but the introduction of the transit method and the launching of the *Kepler* mission revolutionized the field by discovering thousands of planets (Borucki et al. 2010), transforming a once-philosophical query into a statistical and comparative one.

### 1.1 White Dwarf Planetary Systems

Despite the first exoplanets being found around a pulsar, the natural inclination towards finding Earth-like planets around Sun-like stars directed most early

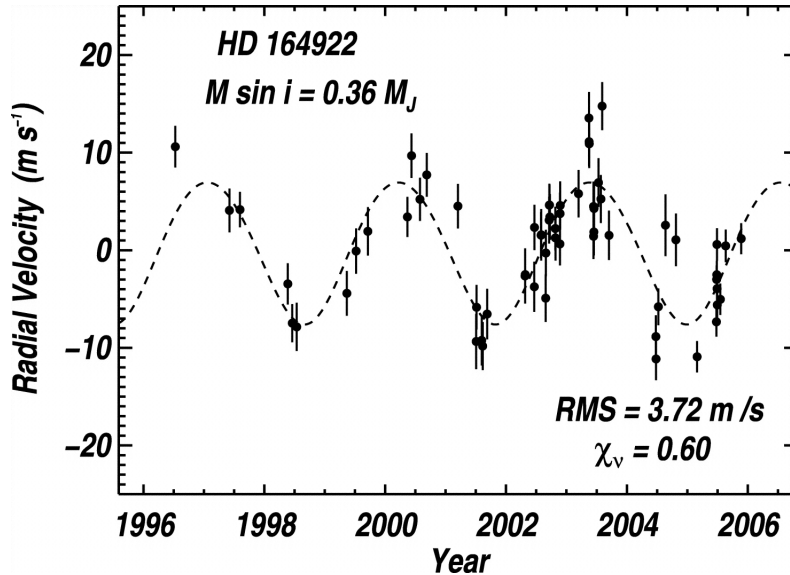


**Figure 1.1:** An example of a radial velocity planet detection: HD164922b, a planet with a lower mass limit of  $M_p \sin i = 0.35 M_{\text{Jup}}$  orbiting a G9V star (Butler et al. 2006).

exoplanet surveys towards main-sequence stars. But despite the absence of detected exoplanets, the number of known white dwarf planetary systems rivals the number of detected exoplanets (Veras 2016a). An estimated 25 – 50% of hydrogen-atmosphere white dwarfs have “polluted” spectra showing the steady accretion of rocky material; evidence of the destruction of a planetary system while a number of these also have dusty disks (Veras 2016a). All white dwarfs with detected disks, a total of nearly 40, are polluted (Farihi 2016). The presence of these heavy metals are not solely due to accretion from the interstellar medium (Kilic & Redfield 2007), though it may contribute. The elemental composition of circumstellar material polluting the white dwarfs roughly resembles chondrites, adding to the evidence of this material being planetary in origin (Jura et al. 2007).

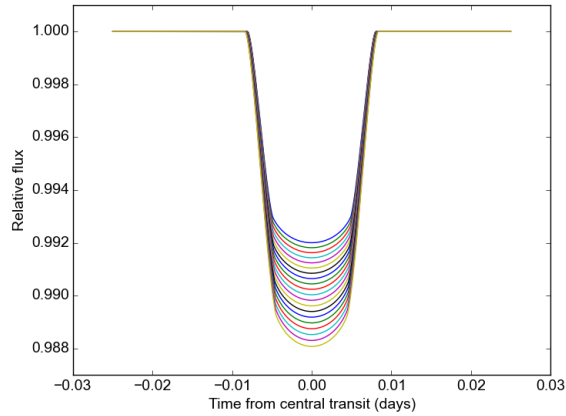


**Figure 1.2:** A demonstration of how increasing  $R_p$  increases the depth of the transit lightcurve. Changing the period, inclination, and eccentricity of the orbit also affect the shape and duration of the transit, although these effects must be considered in concert with the limb-darkening of the star. Image taken from documentation for `batman` (Kreidberg 2015)

## 1.2 White Dwarf Transits

The transit method is relatively cheaper than the RV method for discovering exoplanets because it does not require multiple spectroscopic observations. By keeping track of the flux received from a star, we can watch for small dips if another body crosses the face of the star in between our line-of-sight, such that a small portion of the star’s surface area is obscured by a fraction  $\propto \left(\frac{R_p}{R_\star}\right)^2$ . The transit depth ( $\delta$ ) and knowledge of  $R_\star$  are sufficient to constrain  $R_p$  (see Figure 1.2), and the shape of the light curve helps determine orbital parameters like eccentricity and inclination (Mandel & Agol 2002). Observing these dips periodically help confirm that the signal is genuine though RV followup is usually required to definitively declare that a planet candidate signal is in fact a planet.

The transit method can only detect systems with a favorable geometry at opportune moments, so it requires extensive photometric monitoring to work.

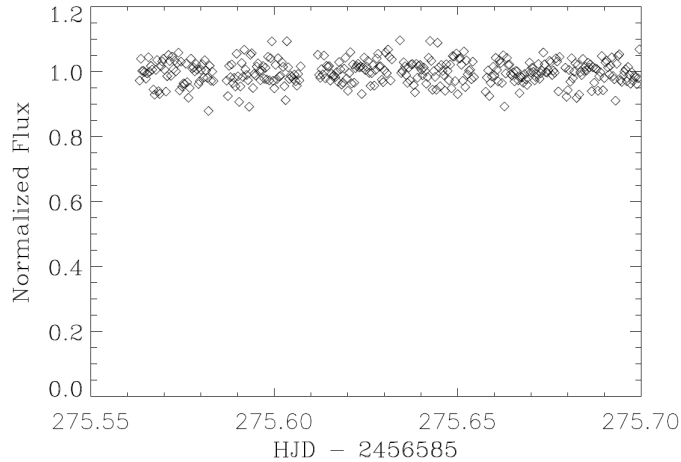


**Figure 1.3:** The 24" Perkin telescope light curve for WD 1208+576 as observed on the 9th of April 2014. We took 20-second exposures with a download time of 10 seconds and used three reference stars to do differential photometry. The total time observed was a little over six hours. A transiting Earth-sized planet in the habitable zone would have caused a  $\sim 80\%$  drop in flux for one or two datapoints, because although the transit depth is very large the transit duration is on the order of minutes.

Unlike the RV method however, transit surveys can search a wide field-of-view and look for planets around many stars at once, which led to the great success of the *Kepler* mission. But the greatest advantage of finding transiting exoplanets is that suitable targets allow us to study their atmospheres using transmission spectroscopy (Seager & Sasselov 1998). A transiting white dwarf planet, should one be found, would be an ideal target because of the small size of the white dwarf (Loeb & Maoz 2013), allowing even a small Mercury-sized planet to have a large transit depth. Furthermore the Goldilocks-zone, or orbital distance at which a planet orbiting a white dwarf may have liquid water on its surface, corresponds to extremely short orbital periods between 5 – 30 hours (Agol 2011).

This motivated us to start a ground-based survey for transiting white dwarf exoplanets using the 24" Perkin Telescope at Wesleyan. A lightcurve representative of our data quality is shown in Figure 1.3, and a plot showing how over only

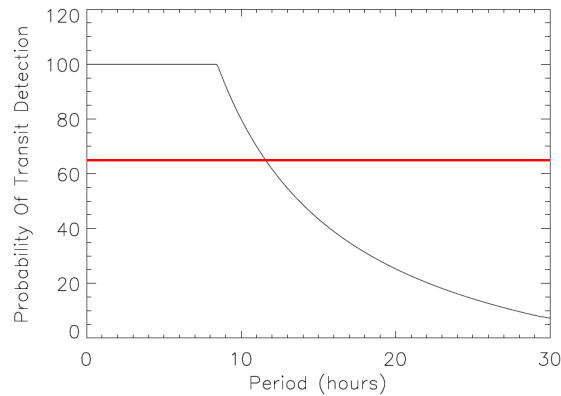


**Figure 1.4:** This is the probability curve for WD 1208 + 576 after 2 nights of observing, 6 and 5 hours long respectively. The overplotted red line marks a detection threshold of 65%. The overall probability that we would have detected a transiting planet is approximately 73%.

two nights of observing we can constrain the probability of a transiting planet to  $< 30\%$  is shown in Figure 1.4. But even with this rapid turnover, the observing conditions in Middletown and irregularity of the observing schedule hinder the survey; with just the  $24''$  program it would take  $\sim 10$  years to constrain the occurrence rate of white dwarf planets to below 25%. But the K2 mission, a revival of the *Kepler* telescope after the failure of its reaction wheels (Howell et al. 2014), allowed us to expand the survey to include white dwarfs in each campaign’s field of view.

### 1.3 Detection of Transits of WD1145+017

K2 lightcurves showed much more systematic noise than the original *Kepler* mission because of the increased drift of the telescope and the periodic thruster-fires to recenter correct for that motion (Vanderburg & Johnson 2014). WD1145+017 was a white dwarf target proposed by multiple groups interested in white dwarf transiting planets, prioritized because it was known to have an

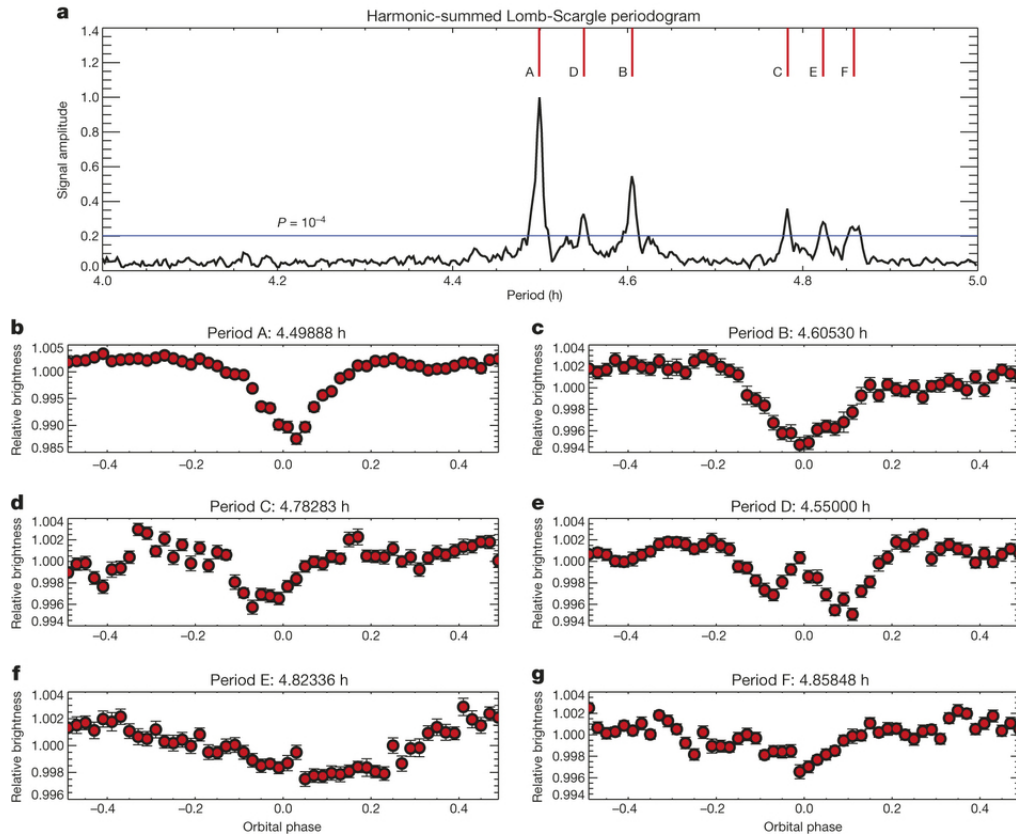


**Figure 1.5:** Vanderburg et al. (2015) found six significant periodicities in the K2 Campaign 1 data for WD1145+017, all  $\sim 4.5$  hours. The phase-folded lightcurves for each period are shown below the harmonic-summed Lomb-Scargle periodogram. The transits are shallow and extended, inconsistent with a solid-body transiting the compact white dwarf.

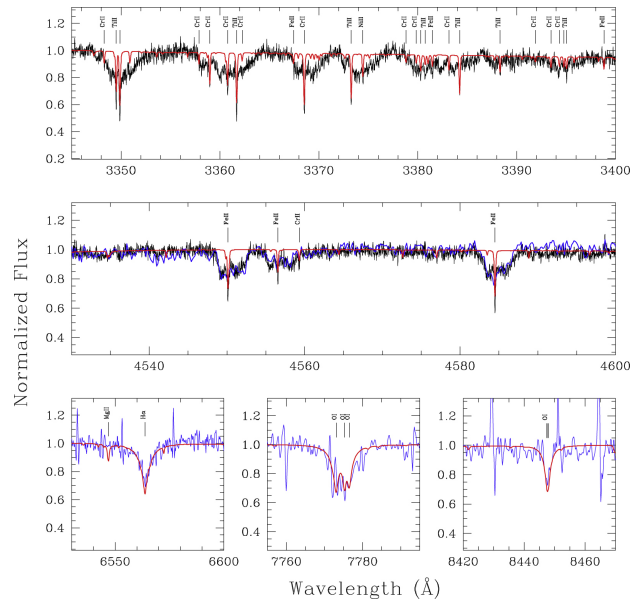


**Figure 1.6:** A large-scale view of the polluted spectrum of WD1145+017 showing circumstellar absorption in multiple lines. A stellar model is shown in red and individual absorption features are labelled by ion. Note that the excess absorption is present on both the blue and red sides of the stellar feature, which did not hold true for later epochs (Figure 1 from Xu et al. (2016)).

infrared-excess indicating the presence of a disk (Xu et al. 2016).

Vanderburg et al. (2015) detected multiple periodic transit signals each with an orbital period  $\sim 4.5$  hours (see Figure 1.5), making WD1145+017 the first white dwarf without a companion to have transiting bodies. The transits were too shallow and long in duration to be caused by a planet, so Vanderburg et al. (2015) proposed that it was a distinegrating minor planet or asteroid (see Figure 1.7), the first such object detected around a post-main-sequence star. A few months later, Xu et al. (2016) found circumstellar absorption in WD1145+017’s spectra, evidence of accretion onto the star (see Figure 1.6). This object presents a unique opportunity to study the death of a planetary system in action, using the remnants and the process of their destruction to probe the interior structure and composition of a planetary body or bodies outside the Solar System; necroplanetology.



**Figure 1.7:** An artist's rendition of a minor planet disintegrating in orbit around WD1145+017. The planet is shown with a comet-like extended tail of gas and dust to explain the irregular shape of the observed transits (from Vanderburg et al. 2015).

# Chapter 2

## Spectroscopy

The majority of white dwarfs have simple spectra that only show lines from hydrogen or helium in their atmospheres. Gravitational settling forces the heavier elements to sink on a timescale of less than  $10^6$  years (Koester 2009), but  $\sim 30\%$  of white dwarfs have spectra “polluted” with metal lines that must have been deposited by relatively recent accretion (Koester et al. 2014). A similar fraction (Koester & Kepler 2015) also have dusty disks thought to be the remnants of the star’s planetary system. Independently of the Vanderburg et al. (2015) detection, Xu et al. (2016) was motivated to spectroscopically observe WD1145+017 because it showed was known to have both a disk and multiple photospheric metal lines. They found circumstellar absorption in transitions from multiple ions (Fe I, Fe II, Ca II, etc.) with a range of oscillation strengths but mostly restricted to low excitation energies ( $< 5$  eV).

The subsequent discovery of irregular transit signatures in *Kepler* K2 data Vanderburg et al. (2015) showed that there were still fragments or dust clouds from a massive body in orbit around the star, prompting follow-up spectroscopic observations to detect variability in the circumstellar absorption (Redfield et al. 2017). The circumstellar lines were found to vary both over the course of a few months between observing runs and also over the course of a few minutes coinciding with a transit signal and leading to a “blueing” of the transit light

curve (Hallakoun et al. 2017).

## 2.1 Datasets

### 2.1.1 *Keck / HIRES*

The High Resolution Echelle Spectrometer (Vogt et al. 1994), or HIRES, on the Keck I telescope was used for multiple datasets in this project. Xu et al. (2016) presented their observations of WD1145+017 obtained with Keck/HIRES under program 15A/UCLA (PI: Jura) and made their data publicly available. They took three 2400 s exposures on the night of 11 April 2015 (UT) with  $R = \Delta\lambda/\lambda \simeq 40,000$ , and a signal-to-noise ratio (SNR)  $> 25$ . Redfield et al. (2017) used the same instrument on 14 November 2015 to observe polluted white dwarfs under program 15B/N116Hb (PI: Redfield). They obtained two 1200 s exposures of WD1145+017 at high airmass with  $R \sim 35,000$  and SNR of 10 across the observed wavelength range of 3100 – 5180 Å.

### 2.1.2 *VLT / X-Shooter*

Under the Director’s Discretionary Time Program 296.C-5014 (PI: Farihi), the X-Shooter intermediate-resolution spectrograph (Vernet et al. 2011) at the ESO Very Large Telescope was used to observe WD1145+017 for three nights: 14 February, 29 March, and 8 April 2016. X-Shooter has three arms: UVB (300 – 500 nm), VIS (500 – 800 nm), and NIR (900 – 2300 nm). For the February run, the exposure times were 300, 366, and  $2 \times 188$  seconds respectively with a total observing time of  $\sim 5.1$  hours. For both the March and April runs, they were 280, 314, and 240 seconds respectively for 2.9 hours in March and 5.0 hours in April.

The SNR for the NIR branch was consistently low ( $< 5$ ) so the data beyond 9000 Å was discounted while the  $R$  was  $\approx 6200, 7450$  for UVB and VIS.

## 2.2 Fitting Circumstellar Absorption (CSA)

To isolate the circumstellar absorption, the stellar component must be removed first. We used a white dwarf atmospheric model fit to the few uncontaminated photospheric lines with a fixed  $T_e = 15900$  K and  $\log g = 8.0$  to maintain consistency with the parameters estimated by the original detection in Vanderburg et al. (2015), but adopt the fitting procedure outlined in Koester et al. (2010). The model matches the photospheric lines in all the datasets closely (see Figure 2.1). The total redshift of the photospheric lines is  $42 \text{ km s}^{-1}$ , with an estimated  $30 \text{ km s}^{-1}$  gravitational redshift (assuming our stellar parameters,  $M_\star = 0.6M_\odot$ ,  $R_\star = 1.4R_\oplus$  are valid) leaving another  $12 \text{ km s}^{-1}$  for the radial velocity of the star. The specific values are irrelevant to modelling the CSA, so any variation due to errors in these estimates have no significant impact.

### 2.2.1 Finding CSA Lines

To find lines with a high amount of CSA, I used the Kurucz Atomic Line Database (Kurucz & Bell 1995) to generate a list of all the transitions with wavelengths within the range of the November Keck data. For each line, I isolated a velocity range of  $-700$  to  $+700 \text{ km s}^{-1}$  from the central wavelength in the rest frame (since the range was so broad, the  $42 \text{ km s}^{-1}$  stellar offset was insignificant) and took all data within that range from each dataset. For each dataset, I subtracted the stellar model, leaving behind only the CSA profile. To determine whether the amount of CSA was significant, I measured the depth of the best-fit

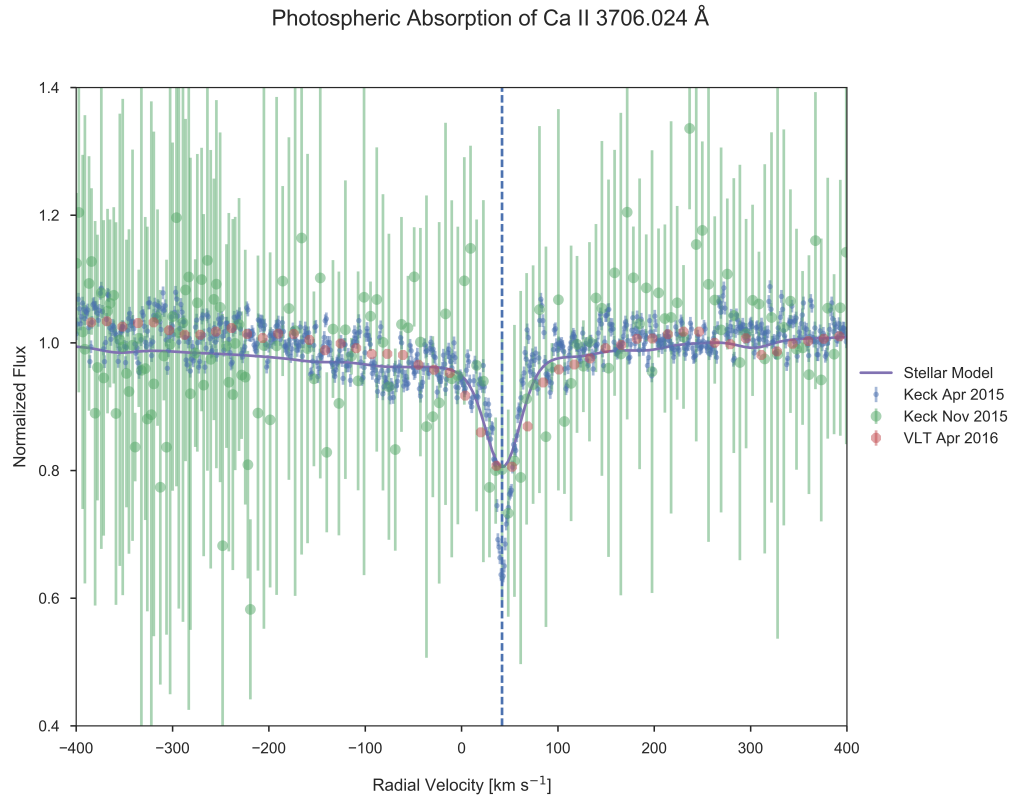


**Figure 2.1:** A comparison between the different datasets at Ca II 3706.024, which only shows photospheric absorption. The purple line represents the stellar model, the light green circles show the November 2015 Keck/HIRES data, the red octagons are the VLT April 2016 X-Shooter data, and the blue points are the April 2015 Keck/HIRES data. The dashed blue line marks the total redshift of  $42 \text{ km s}^{-1}$ . There is no visibly significant excess compared to the stellar model from any of the datasets, and all of them line up well with each other.

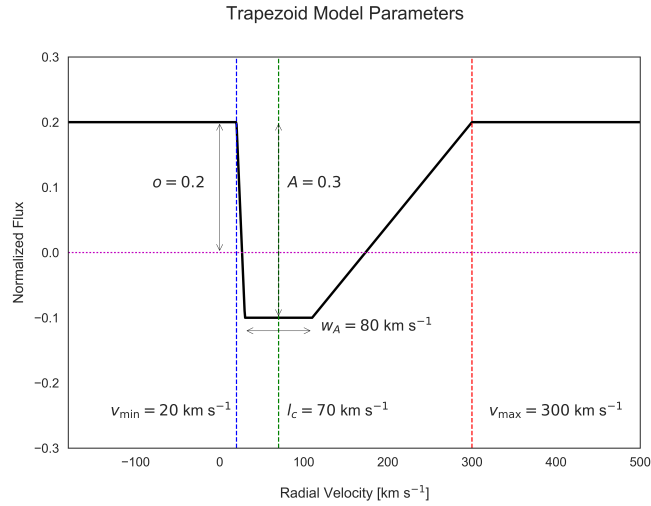


**Figure 2.2:** The trapezoid model used to fit the circumstellar absorption.  $A$  is the amplitude or depth of the trapezoid’s flux absorption, which is offset from 0 by  $o$ . The endpoints of the trapezoid,  $v_{\min, \max}$ , show the boundaries of the absorption and  $w_A$  shows the width of the velocity range for which the feature shows the maximum absorption.

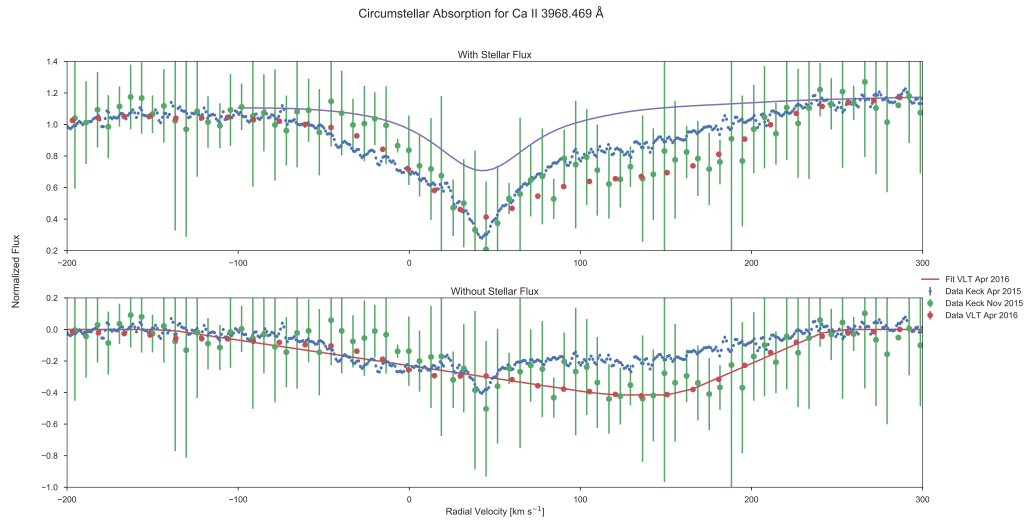


**Figure 2.3:** An example of the trapezoid fitting for the April VLT dataset with the two Keck/HIRES datasets shown for comparison. On top are the three spectra plotted along with the stellar model. Below, the stellar model is subtracted from the data to find the residual absorption. The magenta line shows the best fit trapezoid model for the April VLT data. The CSA extends from about  $-150$  to  $+250 \text{ km s}^{-1}$  with some variability between the different datasets.

trapezoid centered within a restricted range of  $\pm 300 \text{ km s}^{-1}$  of the photospheric line (see Figure 2.2 for a representation of the model parameters and Figure 2.3 for an example of it in action). I compared  $A$ , the depth of the trapezoid, to the standard deviation of the residual absorption after stellar subtraction outside the trapezoid’s range ( $\sigma_{\text{CSA}}$ ). For my preliminary list, I only counted a detection as significant if it  $A > 3\sigma_{\text{CSA}}$  for the November Keck/HIRES data (generally our noisiest dataset). This eliminated the vast majority ( $\sim 90\%$ ) of the lines from the Kurucz database, but to avoid over-counting neighboring lines I manually inspected each tentative detection to ensure that the photospheric contribution lined up perfectly with  $42 \text{ km s}^{-1}$ .

Identifying a smaller subset of features which seemed isolated from blending with other spectral lines, I performed a Markov-Chain Monte Carlo error analysis to fit the trapezoid model to each dataset and determine the errors in my measurements of  $v_{\text{min, max}}$ , which propagate forward to errors in the equivalent width  $W_\lambda$ . The MCMC was implemented with the `emcee` Python package (Foreman-Mackey et al. 2013), an affine-invariant ensemble sampler that uses the Goodman & Weare (2010) modification to the tradition Metropolis-Hastings algorithm.

## 2.2.2 Characterizing CSA Features

We can quantitatively describe a CSA feature with: the equivalent width ( $W_\lambda$ , which gives the total amount of absorption), the velocity range of the feature (the  $v_{\text{min}}$  and  $v_{\text{max}}$  provided by the trapezoid model, which is a proxy for the estimated distance from which the accreting material has been accelerated), and the depth of a feature at a given velocity (which shows the covering fraction of material at that velocity).

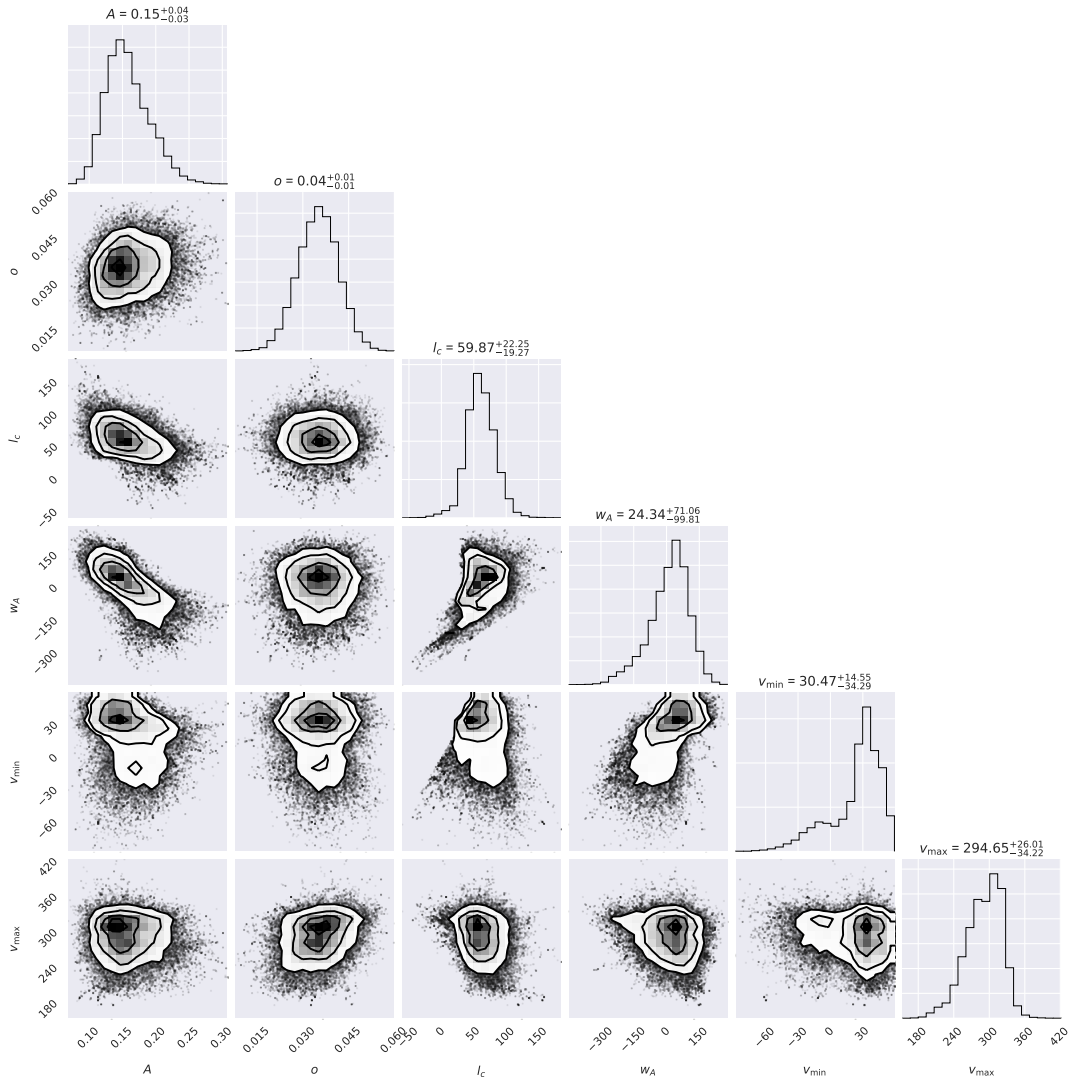


**Figure 2.4:** Posterior samples for the Keck November 2015 dataset, fitting Fe II 4178.862 Å. Units for all parameters match those shown in Figure 2.2:  $A$  [dimensionless normalized flux],  $o$  [dimensionless normalized flux],  $l_c$  [km s<sup>-1</sup>],  $w_A$  [km s<sup>-1</sup>], and  $v_{\min, \max}$  [km s<sup>-1</sup>]. There is some covariance between  $A$  and  $o$ , and it appears that there is lower-likelihood but still significant family of solutions skewing the posterior distributions.

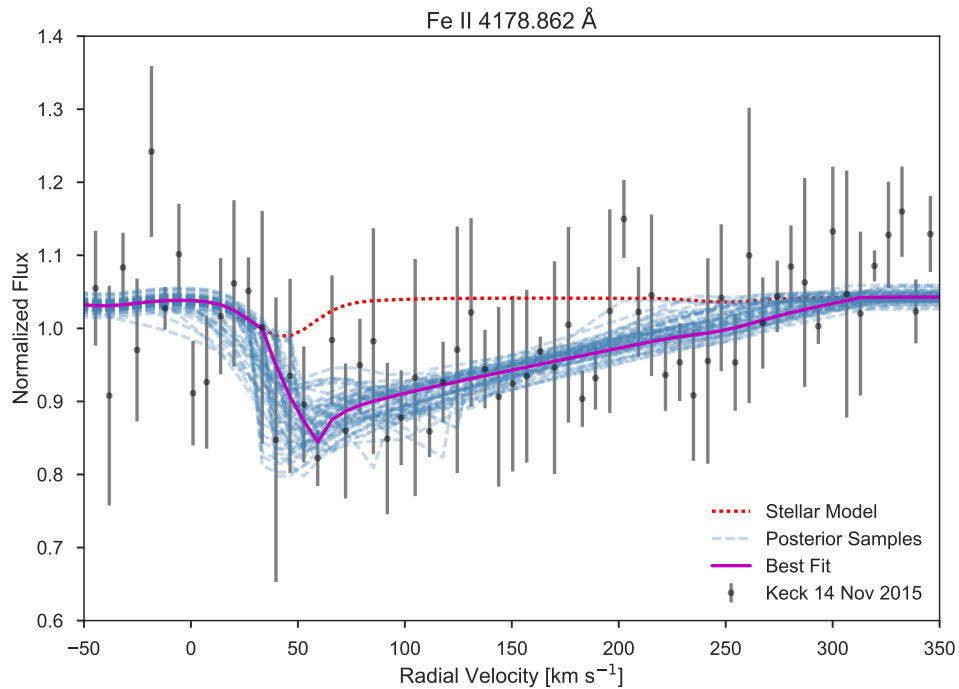


**Figure 2.5:** An alternate representation of the posterior distribution in Figure 2.4. The trapezoid models generated by random samples from the posterior are added to the stellar model and compared to the data along with the best-fit model. The samples are the dashed light blue lines, the best-fit is the purple solid line, the stellar model is shown as a dotted red line, and the data are represented with errors by the black points. The majority of the models show their maximum absorption at  $\sim 45 \text{ km s}^{-1}$ , but the second family of solutions can be seen in the few samples that peak at  $\sim 100 \text{ km s}^{-1}$ .

Looking at the CSA profiles for multiple lines we can show measurable differences in these quantities. The Xu et al. (2016) dataset, which is earliest and most separated in time, shows much more blueshifted absorption ( $\sim 100 \text{ km s}^{-1}$  as opposed to  $\sim 50 \text{ km s}^{-1}$  from the stellar line) than any of the other datasets, while also being weaker on the redshifted side (a difference in depth of  $\sim 0.05$ ). For most lines,  $v_{\text{max}}$  shows a steep cutoff that suggests a well-defined outer radius from which the accreting material is accelerated for all ions (see Figure 2.4).

Figure 2.6 shows the evolution of one circumstellar absorption feature across all epochs. There is a dramatic increase in the total absorption between April and November 2015, with  $v_{\text{max}}$  extending further and  $A$  increasing, but also moving  $v_{\text{min}}$  further to the red. Over the next few months, the absorption contracts again, but both  $v_{\text{min, max}}$  have shifted significantly compared to the initial April 2015 data. Figure 2.7 takes a more global approach to showing the variability; histograms of the trapezoid depth  $A$ , the dimensionless equivalent width  $W = \frac{W_\lambda}{\lambda}$ , and  $v_{\text{min, max}}$  for all isolated CSA features are shown for each epoch.  $W$  and  $A$ , which are closely related, do not have any continuous trends over time, but the centroids of the  $v_{\text{min, max}}$  distributions appear to move slightly to the right and left respectively, suggesting a contraction of the absorption.

The variations indicate that the behavior of the accreting material is changing over a few weeks, though with only a few time-separated datapoints, determining the exact cause of this variation is uncertain (see §2.4 for plausible explanations). The majority of the CSA lines for a given ion are clustered around similarly low excitation energies, suggesting that they are excited at roughly the same orbital distance (Redfield et al. 2017).

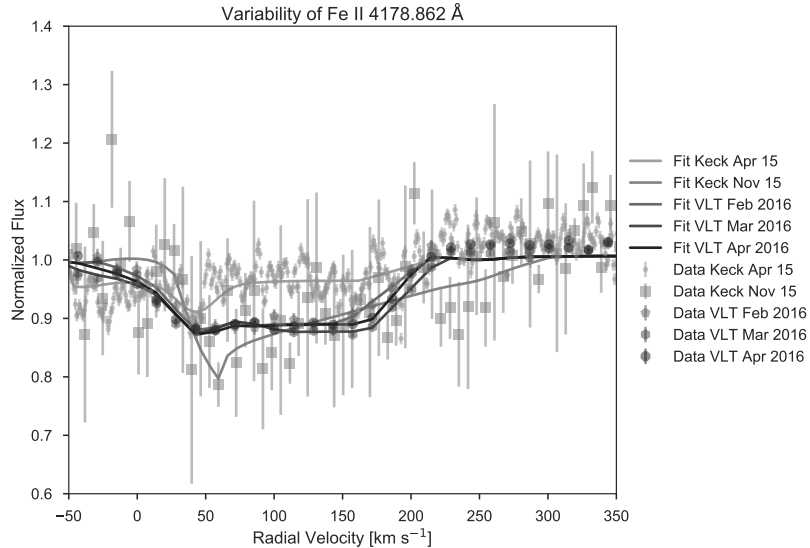


**Figure 2.6:** The CSA across all epochs for one spectral line. The darkness and opacity increase over the course of the year from the Keck April 2015 - VLT April 2016 datasets. This line shows a dramatic increase in absorption between April and November 2015 and then contracts in depth but shifts to a higher velocity range.

## 2.3 CSA Variability

Initially, I could not determine any common trends over time in any parameters that could be attributed to particular physical causes, like the oscillator strength, excitation energy, or ion of the spectral lines. However, after plotting the variation of  $\frac{W}{f}$ , I found a number of lines across ions that seemed to show the same trends. Limiting the sample size to isolated CSA lines with well-fit data across all epochs ( $\sim 30$  lines), I used Agglomerative Clustering implemented in the Python package `scikit-learn` (Pedregosa et al. 2012).

Agglomerative Clustering is a hierarchical method which finds groups in an  $N$ -dimensional parameter space by assigning each sample to a cluster, then joining clusters together in a way that minimizes the total variance. This method worked best because of the uneven cluster sizes and non-Gaussian distribution of this

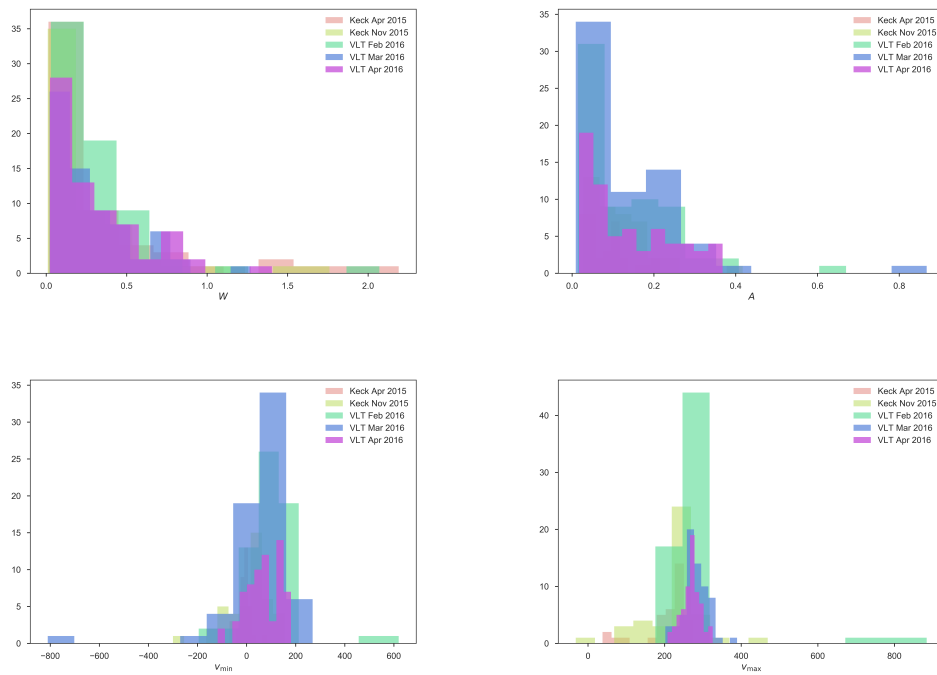


**Figure 2.7:** Each datasets' histogram for  $W$  and trapezoid parameters are plotted to see how these quantities evolve over time. All parameters show a decrease in scatter, which may be a consequence of the higher SNR of the VLT datasets.  $v_{\min}$ ,  $v_{\max}$  show the strongest indication of a time-dependent trend, with shifted centroids across epochs.

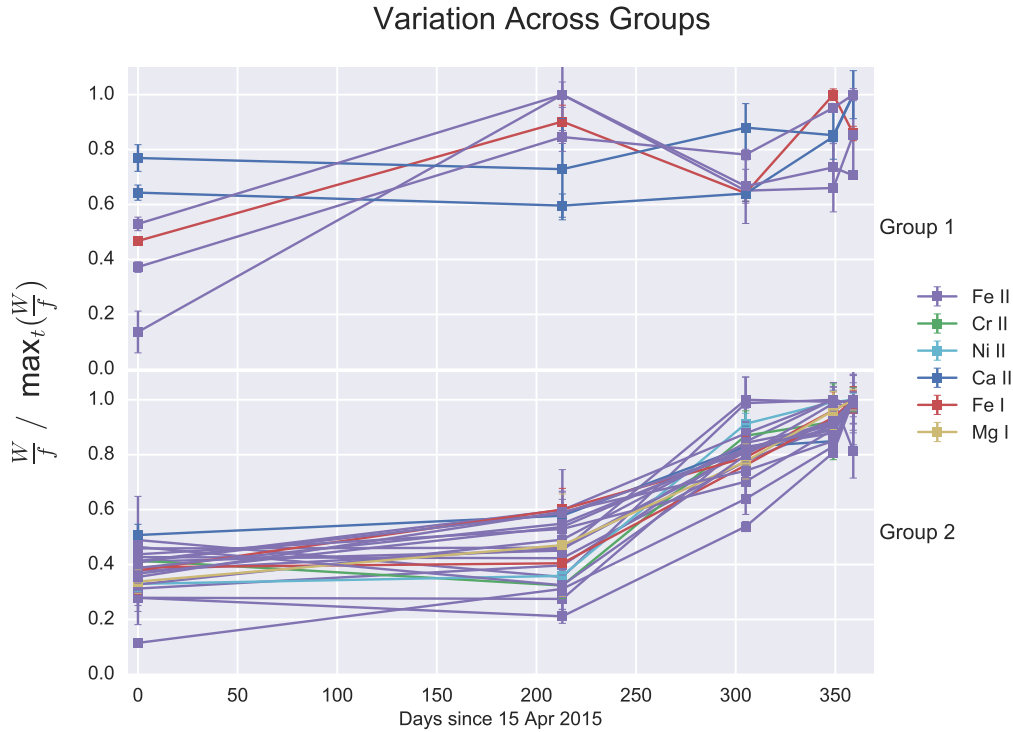


**Figure 2.8:** Identifying two clusters in isolated CSA lines with well-fit data for all epochs. Group 2 shows coherent behavior, but Group 1 appears to simply be the complement of Group 2 without much to unify it other than the high absorption in the November 2015 epoch.

particular parameter space ( $\frac{W}{f}$  across all 5 epochs). To incorporate the errors, I ran the algorithm on multiple samplings of each observation, but the same groupings were assigned consistently.

This identified two main groups where the most distinguishing feature was the change in CSA from April 2015 to November 2015. For the smaller group, with only 6 lines, there was a dramatic change in absorption between these two epochs and only marginal changes afterward. Group 2 however, did not change very much over that time period, but increased between November 2015, March 2016, and Feb 2016 with a relatively constant slope. Both groups showed little change between the most closely spaced epochs, March and April 2016, suggesting that the

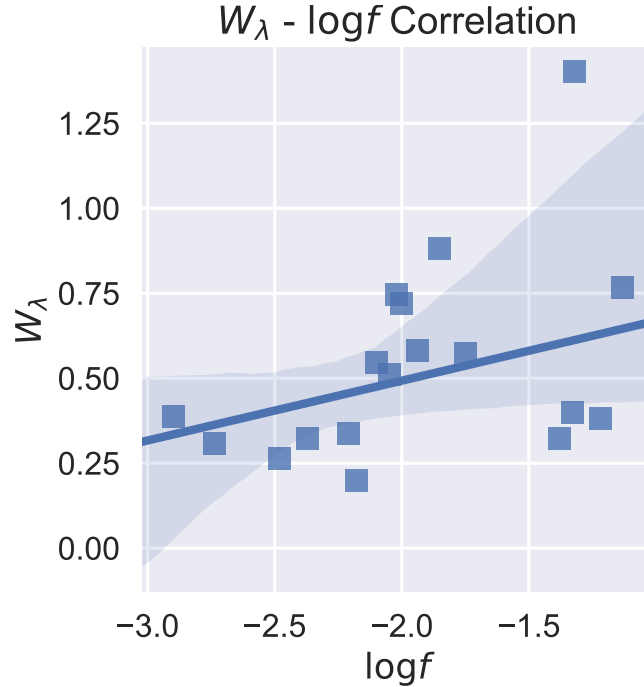


**Figure 2.9:** Plotting the equivalent width  $W_\lambda$  against the oscillator strength  $\log f$  for all Fe II lines in Group 2, we see a roughly linear correlation. The blue line shows the best fit line while the shaded region is the  $1\sigma$  error in the fit. Redfield et al. (2017) use this correlation to find the optical depth  $\tau \approx 2.0$ .

changes are dominated by steady processes. The clustering method did not find significant results with any other parameters and there were no identifiable trends to distinguish these groups by ion,  $f$ , or  $E_l$ . Perhaps Group 1 was contaminated by other lines that I could not identify by eye or using the Kurucz database. The coherent behavior of Group 2 implies that the absorption from those lines is from the same source, so an alternate explanation is that the lines in Group 2 were affected by another source.

The equivalent width  $W_\lambda$  and the optical depth  $\tau$  can be used to calculate the column densities,  $N_l$ , for ions independently for each spectral line with circumstellar absorption.  $N_l$  measures the number of absorbers for that ion along the

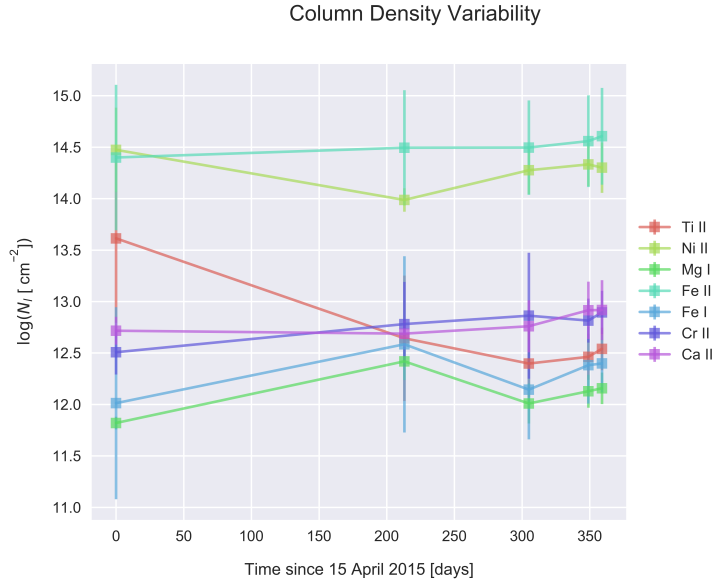


**Figure 2.10:** Variability of  $N_l$  over time. Fe and Ca are enhanced compared to the other elements which Redfield et al. (2017) argue indicates the presence of both core and crust-like material.

line of sight

$$N_l = \frac{W_\lambda}{f\lambda^2} \times \left(1 + \frac{\tau}{2\sqrt{2}}\right) \times 1.130 \times 10^{12} \text{ cm}^{-2} \quad (2.1)$$

where  $f$  is the oscillator strength of the line. This is an approximation derived by assuming a low  $\tau$  and Gaussian profile for the absorption line (Draine 2011). The formula is accurate to within 2.6% for  $\tau < 1.254$ , but Redfield et al. (2017) estimate the median  $\tau \approx 2$  (see Figure 2.9) and our circumstellar absorption is not strictly Gaussian, so the errors for  $N_l$  will be much greater than the propagated values. Using the measurements from multiple epochs and averaging over all the lines for each element, we can see both the relative abundances of these elements and their changes over time (see Figure 2.10). The standard deviation of  $N_l$  for all lines of a given ion at a single epoch are used for the errors in lieu of the propagated errors.

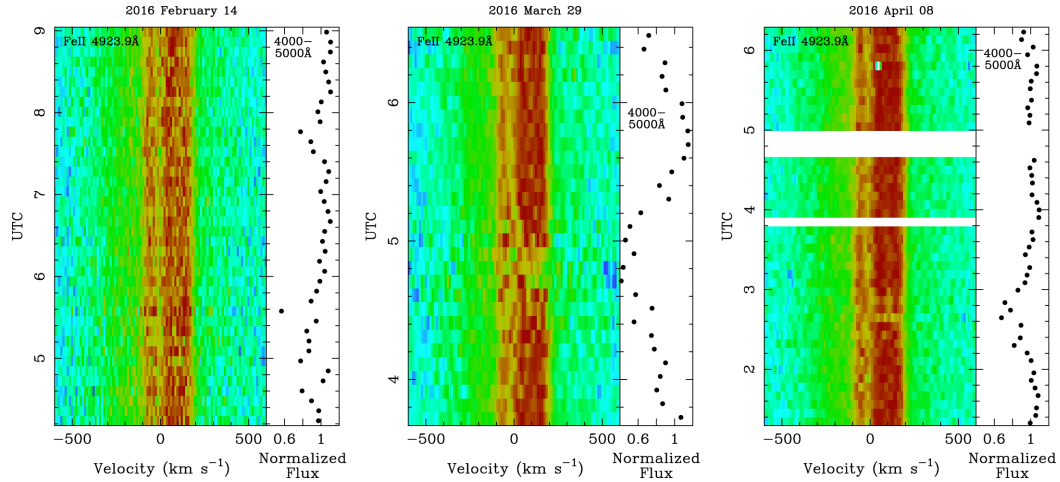


**Figure 2.11:** Figure 5 from Redfield et al. (2017), showing the circumstellar absorption for Fe II 4923.9 Å during three epochs from left to right: 14 February, 29 March, and 8 April 2016. All data were taken using VLT/X-Shooter. The narrow panel to the right of each subfigure shows spectrophotometry of a broad 4000 - 5000 Å range. Green values indicate flux at the level of the continuum while red indicates absorption in flux. The darkest regions correspond to drops in flux  $\sim 40\%$  and time is shown increasing along the  $y$  axis. While the February data is roughly constant over time, both the March and April data show a change in the flux over the course of a few minutes coincident with transit events detected by photometric monitoring from other groups.

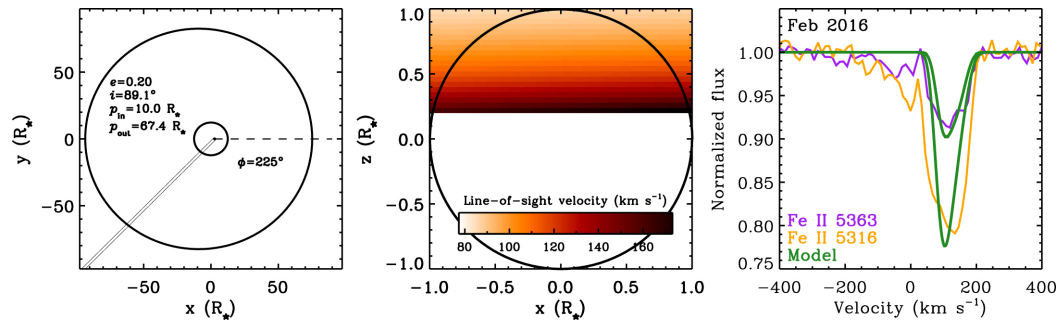


**Figure 2.12:** Figure 6 from Redfield et al. (2017) showing a low eccentricity, slightly inclined disk model. The left panel shows the geometry of the disk: its radial extent from  $10R_*$  -  $90R_*$ , and orientation relative to our line of sight. The middle panel shows the radial velocity projected along our line of sight against the face of the star. The panel on the right shows the VLT April 2016 data for two Fe II absorption features and the model's predicted circumstellar absorption. Note that the structural features are well reproduced, though this would not hold true for the Keck April 2015 data because of the observed blue-shifted absorption.

## 2.4 Disk Modeling

The presence of minute-scale variability related to the transits (see Figure 2.11) helps constrain the geometry of the system because the transiting debris is acting as an opaque object blocking our view of the circumstellar gas absorption. This means that the accreting gas must be interior to the 4.5 hour orbit of the transiting material. To explain the observed variability, both on the minute and month scales, Redfield et al. (2017) propose an eccentric disk with a slight inclination. By populating this disk with gas and assuming a Doppler-broadened delta function profile for absorption lines with  $15 \text{ km s}^{-1}$  intrinsic line broadening, this model can reproduce the structure of the observed circumstellar absorption (see Figure 2.12).

The long-term variability is possibly due to general relativity induced precession of different parts of the debris disk occurring at different rates, changing the total amount and velocity distribution of material in the accretion disk along the line of sight (Veras 2016b). Density variations within the disk, stirred up by material from the transiting debris, can also change the observed amplitudes of the absorption. This model does not provide an explanation for the observed blue-shifted absorption present in the April 2015 Keck data, but this could be explained by magnetospheric accretion that is stochastic in strength (Redfield et al. 2017). The minute-scale variability is simply caused by the opaque transiting bodies obscuring part of the disk along our line of sight.

# Chapter 3

## Stability

The disk model suggested in Redfield et al. (2017) is different from the dusty disk causing the infrared excess described in Vanderburg et al. (2015) and Xu et al. (2016). At  $10 - 67.4 R_*$ , this disk is too close to the host star to be directly detected. But if it exists and is warped as Redfield et al. (2017) describe, it must be related to the transiting bodies detected by Vanderburg et al. (2015). Understanding the geometry of the system to satisfactorily explain both the spectroscopic and photometric observations requires simulating these planetary bodies to determine their orbital architectures.

### 3.1 Constraints on Mass, Eccentricity, $N_f$

Early observations of the WD1145+017 system found one dominant periodicity at 4.5004 hours and six other smaller ones in shorter periods (Vanderburg et al. 2015). This motivated Gurri et al. (2017) to constrain the mass and eccentricity of the system with the condition that the configuration remain stable over at least 2 years, roughly the minimum baseline established by observations. Their work employed a number of approximations to limit phase-space, such as initializing all the smaller “fragments” of the parent body at the same orbital period, 4.493 hours and fixing the number of fragments at six. They also characterized instability by finding the maximum deviation of a fragment’s orbital period com-

pared to its original value, assuming that this  $\langle \Delta T_{\max} \rangle$  would be less than the standard deviation of the shorter periods to be consistent with observations. Due to computational concerns, they also limited their integration time to 5 years. Continued observation of the WD1145+017 system has shown an evolution from relatively shallow signals with distinct periods closely spaced together in phase to a much more active state of continuous obscuration. Some consistent signals can be identified (see Chapter 5), but many transits appear to be superpositions of individual bodies. Here I revisit the simulations of Gurri et al. (2017) but relax their constraints to find what conditions can satisfactorily explain this evolution.

### 3.1.1 Simulation Parameters

My three independent variables along with the findings from Gurri et al. (2017) in parentheses are:

- $10^{18} < M_b < 10^{23}$  kg = the bulk mass of the parent body ( $10^{18} - 10^{22}$  kg)
- $0 < e < 0.1$  = the eccentricity (dependent on mass, but likely  $< 10^{-3}$ )
- $6 \leq N_f \leq 8$  = the number of fragments (fixed at 6)

The parent body is given a radius according to a uniform density distribution between  $3 - 4$  g cm $^{-3}$  as per the constraints of Veras et al. (2017). The fragment masses are allowed to vary uniformly between  $0.2 - 0.001 \times M_b$ , with densities between  $0.2 - 1.3 \times \rho_b$ . The fragments are given initial periods between 4.490 and 4.495 hours to better match the initial observed periods, though interactions quickly change these values. For every combination of the 3 independent variables, 5 simulations are run with different seeds for up to 10 years. Collisions are resolved by highly inelastic collisions with a coefficient of restitution = 0.3, justified by the

assumption that these fragments are no longer coherent objects but are better described as weakly bound aggregates.

REBOUND offers multiple integrators to solve the N-body gravity problem, described further in §A.2. LEAPFROG is a second-order modified Euler scheme, WHFAST is a symplectic integrator that uses a modified Wisdom-Holmann mapping Wisdom & Holman (1991), and IAS15 is a predictor-corrector method with adaptive timestepping. HERMES is a hybrid integrator that combines both IAS15 and WHFAST, preferring WHFAST when bodies are further than 3 Hill radii from each other and switches IAS15 to resolve close encounters and collisions.

By calculating the total energy of the system every timestep and comparing it to the initial conditions, different integrators can be compared by their ability to conserve energy given the same physical scenario. This metric is not an absolute measure of ‘quality’, but it can point out unusual behaviors specific to each integrator. For one set of simulation parameters, I tested each of these integrators over 2000 days to see which had the least energy error and found that collisions had a significant impact on the error trend for each integrator. LEAPFROG’s error goes through high amplitude oscillations (compared to the other integrators, but still of order  $10^{-6}$ ) that change period after a collision. In the absence of collisions WHFAST and HERMES are both extremely stable, but after each collision the error jumps dramatically. IAS15 also shows shifts after collisions, but these are much smaller,  $\sim 10^{-13}$ , so it is the most stable. For all the simulations outlined here, I used IAS15 with an initial timestep of 10 seconds.

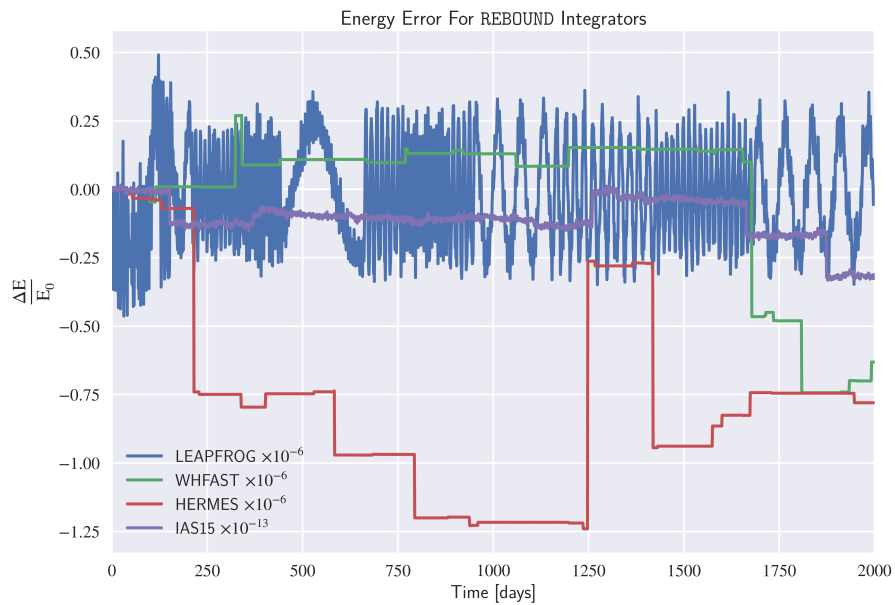


**Figure 3.1:** Using a randomly selected set of initial conditions from the parameter space described in §3.1.1, different integrators were tested to find their energy errors. IAS15 shows the best performance, with an error  $\sim 10^{-7}$  better than the others. All show irregular behavior corresponding to close encounters or collisions, but although this manifests differently between integrators, IAS15 still shows the most stable performance.

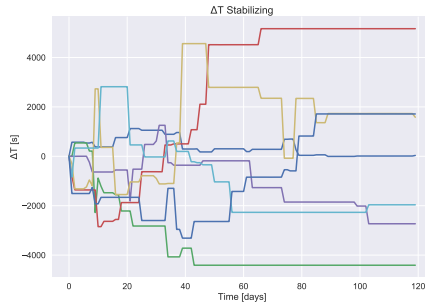


**Figure 3.2:** An example of how, despite initially chaotic  $\sim 1$  hour oscillations in the orbital period, fragments can stabilize to relatively fixed orbits.

### 3.1.2 Characterizing Instability

For instability we use the same metric as Gurri et al. (2017),  $\langle \Delta T_{\max} \rangle$ , defined as the average of

$$\Delta T_{\max} = \max_{\text{frag}} |T(t) - T(t = 0)| \quad (3.1)$$

where “frag” runs over all fragments in the simulation, for all simulations with the same parameters. This describes the total period deviation of fragments compared to their original position; large changes over short periods of time indicate that the orbital architecture is not stable.

I did not fix any threshold value for instability, though larger values do map to less dynamically stable systems. For multiple cases, I found that an initially chaotic period with high amplitudes of  $\langle \Delta T_{\max} \rangle \approx 1$  hour oscillating every few days eventually settled down to steady states after  $\sim 100$  days (see Figure 3.2). In addition, the simulations demonstrated that collisions can induce inclinations in otherwise planar systems, but do not necessarily eject bodies from the system (see Figure 3.3).

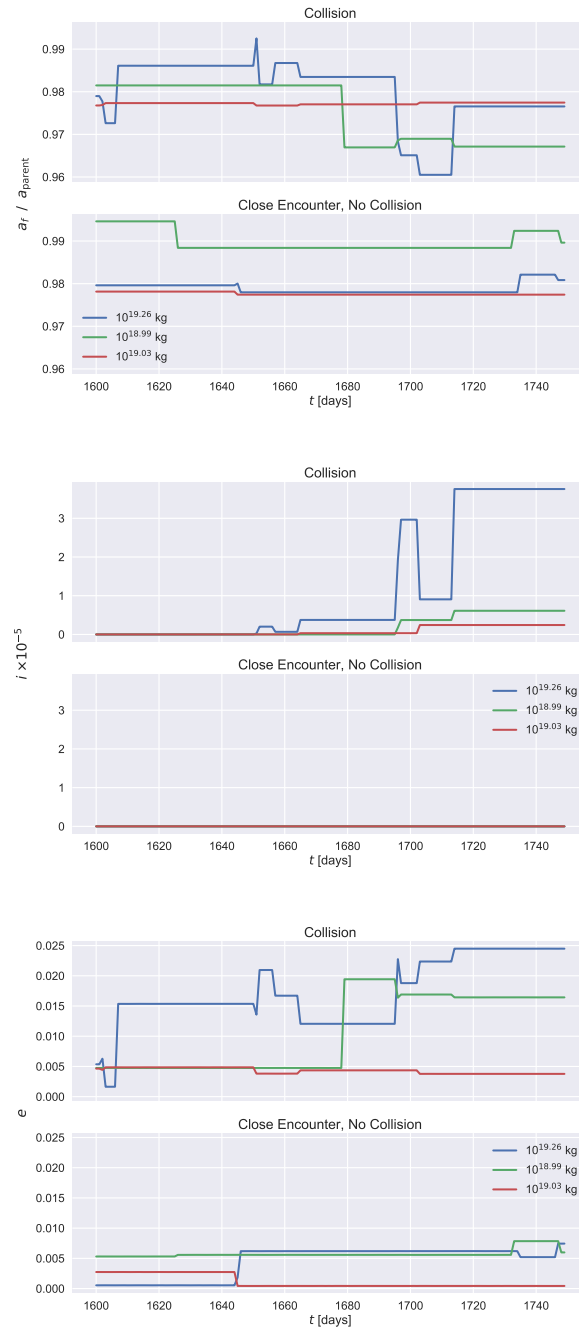


**Figure 3.3:** Collisions and close encounters both affect  $e$  and  $a$ , but only a collision can kick a fragment out of the orbital plane into an inclined orbit. The low coefficient of restitution allows these events to occur without ejecting fragments entirely. Both simulations have the same simulation parameters described in §3.1.1 but have different random seeds, allowing for different initial conditions.

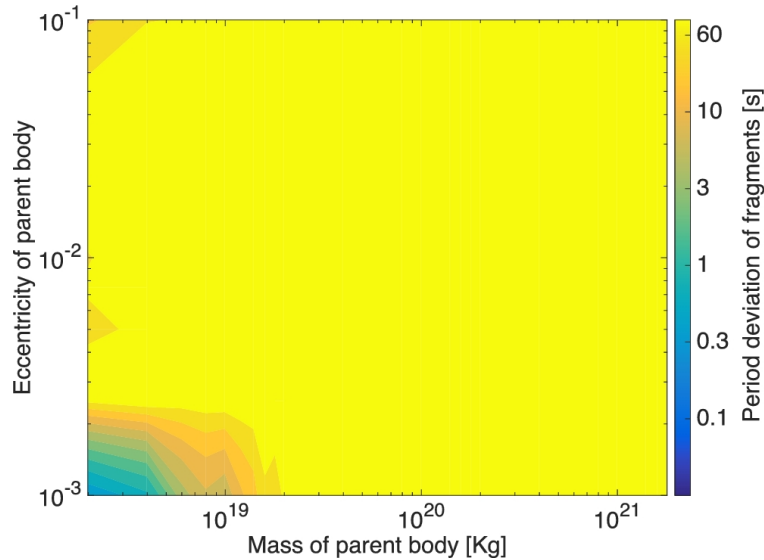


**Figure 3.4:** Figure 3 from Gurri et al. (2017) showing regions of stability after 2 year-long simulations.  $M_b$  and  $e$  are logarithmically spaced by 15 and 20 values respectively, with each pixel averaged over 50 simulations. They identify a very small region of parameter space with low  $M_b$  and  $e$

## 3.2 Implications for WD1145+017

Initial observations showed that the transits of different periodic signals were closely spaced, differing only by a few seconds relative to the dominant “parent body” transit. Gurri et al. (2017) defined their stability criterion accordingly and placed their constraints at  $\sim 6$  seconds. With our relaxed constraints on the fragments’ initial periods, there are more opportunities for interactions influencing their orbits. This leads to much greater period  $\langle \Delta T_{\max} \rangle$  values than Gurri et al. (2017) observed (we mark all  $\langle \Delta T_{\max} \rangle > 60$  seconds as equally unstable to compare to Figure 3.4), but the lower ends of our mass and eccentricity intervals are comparable across all choices of  $N_f$ , though those choices change the structure slightly (see Figure 3.5. These differences may vanish or become more apparent if averaged over more runs, but the overlap between both Figures 3.4 and 3.5 at

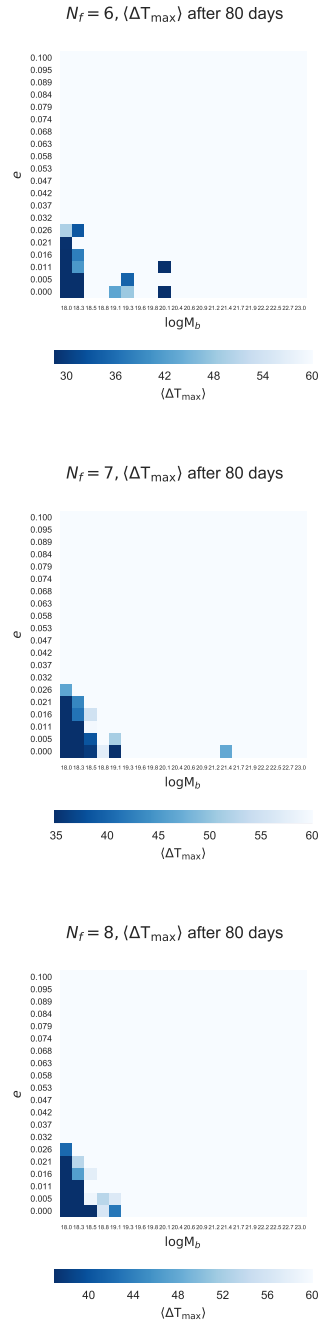


**Figure 3.5:** Stability regions for different values of  $N_f$  after 80 days, assuming that any simulations with  $\Delta T$  values over 60 seconds are unstable or inconsistent with observations.  $M_b$  is logarithmically spaced between  $10^{18-23}$  and  $e$  is linearly spaced between 0.0–0.1 in 20 bins each. The value for a pixel is averaged over 5 simulations with different random seeds.

low  $M_b$ ,  $e$  holds true across all tested values of  $N_f$ .

However, followup observations showed these periods drifting, separated by minutes and eventually hours, until no photometrically “quiet” time remained. Gurri et al. (2017) showed that their simulation parameters led to stable conditions over 5 years with these small period variations, which fails to satisfy observational constraints. Here we allow our simulations to evolve and display stability maps at 5 and 10 years, marking any simulations with  $\langle \Delta T_{\max} \rangle > 900, 4500$  seconds for both epochs respectively as unstable (see Figures 3.6 and 3.7). Our simulations are more consistent with observations precisely because they are less stable, though the degeneracy between different values of  $N_f$  persists. This suggests that as long as collisions are inelastic and the fragments are sufficiently low mass, the number of fragments does not matter much.

The number of periodic signals found in the photometry for WD1145+017, some of which appear and disappear (discussed further in Chapter 5), suggest that many bodies must be present but that this need not lead to a short-lived system. Additionally, our results slightly shrink the mass constraints of Gurri et al. (2017), suggesting that the parent body has a  $M_b \sim 10^{18-19}$  kg (10 – 100  $\times$  the mass of Ida) but expand the eccentricity upper bound to  $e < 0.02$ .

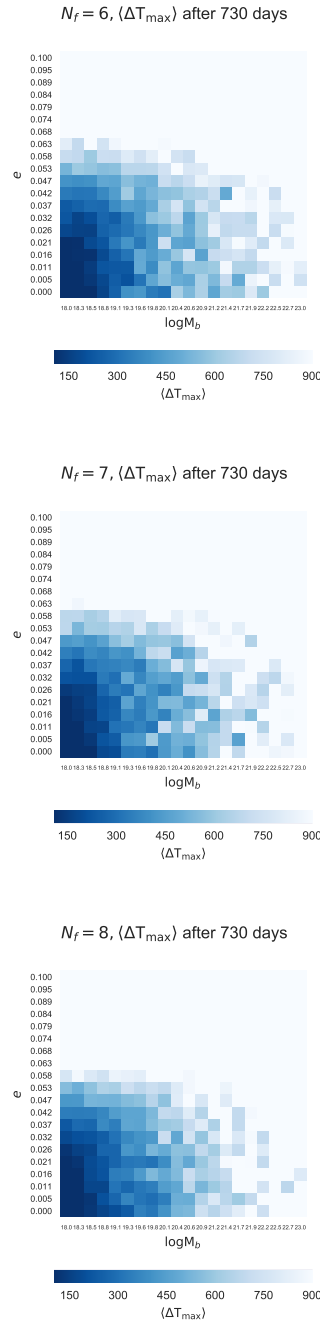


**Figure 3.6:** Stability regions for different values of  $N_f$  after 730 days ( $\sim 2$  years), assuming that any simulations with  $\Delta T$  values over 900 seconds are unstable or inconsistent with observations. Simulation parameters are identical to Figure 3.5

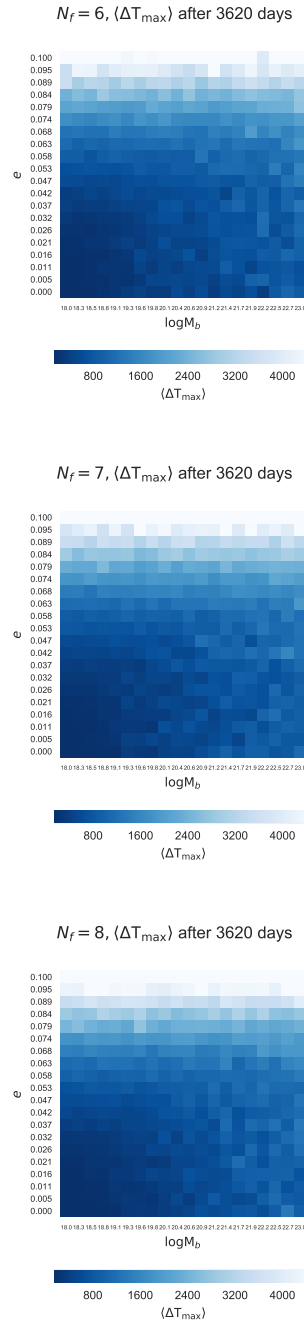


**Figure 3.7:** Stability regions for different values of  $N_f$  after 3620 days ( $\sim 10$  years), assuming that any simulations with  $\Delta T$  values over 4500 seconds are unstable or inconsistent with observations. Simulation parameters are identical to Figure 3.5

# Chapter 4

## Disruption

In the previous chapter, we assumed that the fragments would behave like loosely bound debris clouds, motivated by the extended transits seen in the photometry. By simulating the tidal disruption of differently structured bodies, we hope to replicate the observed trends in the photometry. Veras et al. (2017) explored the asteroid structures required to disrupt slowly enough to remain observable but limited their parameter space by assuming that the asteroid was either homogenous or differentiated into two layers with a fixed core volume fraction = 0.35 and ratio between the core and mantle = 0.25. These choices have precedent in Leinhardt et al. (2012) and Veras et al. (2014), but we show that changing these parameters leads to observably distinct results.

### 4.1 Rubble Piles

Studies of Near-Earth Asteroids have shown that many are well-described by gravitational aggregates; particles clumped together by gravity in irregular shapes created when collisions are too slow to cause fragmentation. Pictures obtained of boulders stuck to the surface of Itokawa, the smallest asteroid visited by a spacecraft, creating a “sea-otter” shaped asteroid, motivated Michel & Richardson (2013) to perform numerical simulations analyzing the material properties and dynamical scenarios required to form such bodies. They found that for a

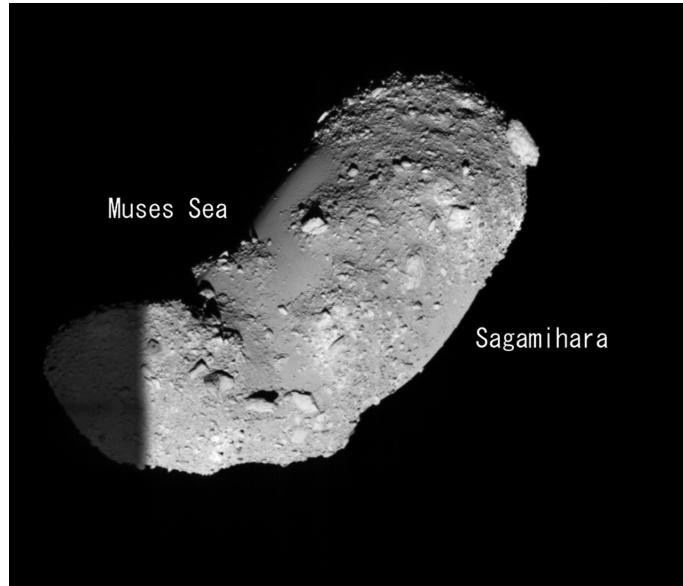


**Figure 4.1:** Figure 2 from Fujiwara et al. (2006) showing an image of the rubble-pile asteroid Itokawa taken by the Hayabusa spacecraft taken on 18 October 2005

certain range of low bulk densities and high material strengths, Itokawa-like bodies with collisional lifetimes  $< 1$  Gyr could be formed (see Figures 4.1 and 4.2). For higher densities, asteroids reshape themselves more compactly and for lower strengths, where collisions remove fragments more easily, both processes lead to more spherical bodies. Accordingly, we felt it was safe to share the assumptions of Veras et al. (2017) that the planetary body or bodies orbiting WD1145+017 were spherical rubble piles.

#### 4.1.1 Hexagonal and Random Packing

Initializing the spherical object as a collection of smaller particles required assuming that the particles were distributed in some way. Assigning a purely random position within the sphere, with a uniform distribution of  $r$ ,  $\sin \phi$ , and  $\cos \theta$  allows particles to overlap. REBOUND would interpret this as a collision which might resolve itself in an unphysical way. Another consideration is that while

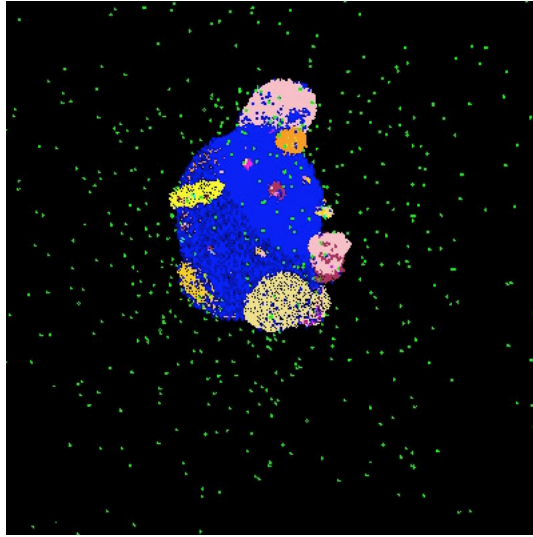


**Figure 4.2:** By removing the assumption that particles merge to form larger spherical particles, Michel & Richardson (2013) simulated formation scenarios for aggregates like Itokawa, but found that these were easily reshaped into approximate spheres by collisions and self-gravity.

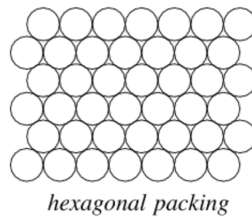


**Figure 4.3:** Hexagonal Packing (Steinhaus 1999, p. 202). This is one of 2 packing methods to maximally occupy a volume with equally sized circles or spheres.

the particles are distributed within the spherical volume we have prescribed, the density must be relatively uniform within that volume and approximate a single sphere as closely as possible. The Kepler conjecture, first proposed by Kepler in 1611 and then formally proven in Hales et al. (2015), states that no arrangement of spherical particles within a volume can occupy a fraction of it  $> \frac{\pi}{3\sqrt{2}} \approx 0.7405$ . The maximal packing methods are the close-packed and hexagonal-packing methods (see Figure 4.3). This regular packing tends to be harder to disrupt than random packings, but be less physically realistic for asteroids, so most tidal disruption

simulations opt for random-packing algorithms instead.

### 4.1.2 Force-Biased Algorithm

I used the force-biased algorithm developed by Mociski et al. (1989)<sup>1</sup> and described in Baranau & Tallarek (2014).  $N$  spherical particles are defined with individual radii (for convenience, I made all particles equivalent with a dimensionless radius of 1) within a box whose volume far exceeds the total volume of the spheres. In consecutive steps, the box contracts at a defined rate and particles are shifted to remain within the box. In addition to their physical radii, all particles have a slightly larger radius of influence ( $R_F \sim 1.1R$ ). If after a step, the forced contraction of particles puts two within each others' radii of influence, both experience a repulsive force with magnitude,

$$f = |k \times (r_o^2 - 4R_F^2)|, \quad (4.1)$$

where  $k$  is a scaling constant and  $r_o$  is the radius of overlap between the two spheres (adapted from Donev et al. (2004), see Figure 4.4), forcing them to move apart. The process repeats until the contraction is no longer possible; when the particles are “jammed” together with nowhere to move. Packings generated with this method tend to have a volume occupation fraction of  $\sim 0.65$ , though they approach the Kepler conjecture limit for small values of  $N$  (Mociski et al. 1989). Figure 4.4 shows this process after the box has contracted enough to force all particles to come into contact with each other. Arrows mark the direction and magnitude of the force a particle is experiencing. Note how the particles in the top and bottom left corners are “jammed”; unable to move because they are trapped

<sup>1</sup>Implemented in <https://github.com/VasiliBaranov/packing-generation>

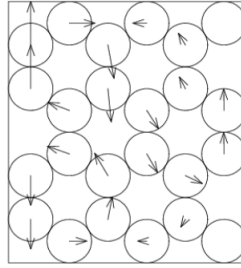


**Figure 4.4:** Force-Biased Algorithm, Figure 4.4 in Donev et al. (2004)

by the corner and another particle perfectly opposite to the corner.

I then find the side-length of the cube,  $s$  and keep only those particles within the sphere of diameter  $s$ . Using different random seeds I generated 100 such random sphere packings to use in my simulations, avoiding the computational cost of generating a new packing for every simulation. Every time a rubble pile is initialized, a saved packing is randomly chosen. To test reproducibility and the effect of individual packings on my results, I can fix the random seed before a packing is chosen.

### 4.1.3 Rubble Pile Parameters

To create a differentiated rubble pile, I need to define:

- $M_b$  = the total mass
- $\rho_b$  = the bulk density
- $f_c$  = the volume fraction (or fraction of total particles) occupied by the core
- $f_m$  = the volume fraction of the mantle
- $k_m$  = the density of the mantle relative to the core (always  $< 1.0$ )
- $f_l$  = the volume fraction of the crust (0 for a two-layered body)

| $f_c$ | $k_m$ | $f_m$ | $k_l$ | $f_l$ | Description                                 |
|-------|-------|-------|-------|-------|---|
| 0.35  | 0.27  | 0.65  | 0.0   | 0.0   | Ceres-like: Icy Mantle, Large Core          |
| 0.15  | 0.27  | 0.85  | 0.0   | 0.0   | Callisto-like: Icy Mantle, Small Core       |
| 0.35  | 0.43  | 0.65  | 0.0   | 0.0   | Rocky Mantle, Large Core                    |
| 0.15  | 0.43  | 0.85  | 0.0   | 0.0   | Moon-like: Rocky Mantle, Small Core         |
| 0.35  | 0.43  | 0.35  | 0.1   | 0.3   | Rocky Mantle, Crust, Large Core             |
| 0.15  | 0.43  | 0.55  | 0.1   | 0.3   | Vesta-like: Rocky Mantle, Crust, Small Core |

**Table 4.1:** Example Rubble Pile Structures shown in Figure 4.5

- $k_l$  = the density of the crust relative to the core (only needed if  $f_l > 0$ , always less than  $k_m$ )

Defining any 2 of  $f$  is sufficient to constrain the third since they must sum to 1. These parameters translate to assumptions about the internal structure and composition of the objects being disrupted by WD1145+017, which would hopefully allow us to constrain information about the interiors of planetary bodies outside the solar system. This only works if the disruption simulations indicate observable differences in the timescale and nature of disruption. Figure 4.5 shows six different such structures:

Given  $M_b$  and  $\rho_b$ , I can find the radius  $R_b$  and scale all particles from the random packing appropriately. Masses are assigned to each particle depending on their location within the sphere according to the density ratios  $k$  and the radii limits defined by the volume fractions  $f$ . Any arbitrary value for the mass of an individual particle works as long as the ratios between layers are maintained, because at the end the mass of every particle is scaled by the same constant to ensure that  $M_{\text{tot}}$  of all particles sums to  $M_b$ .

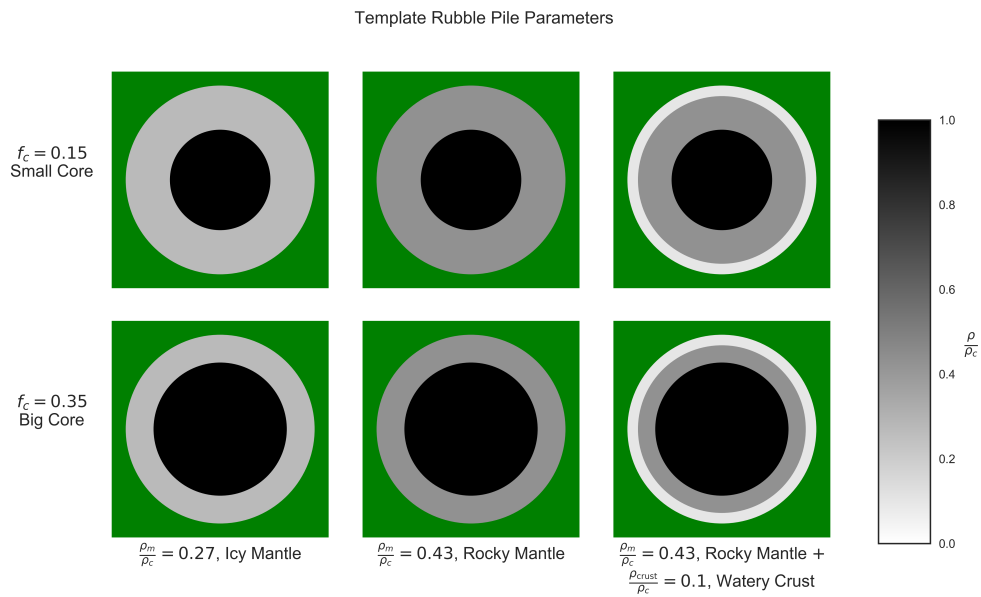


**Figure 4.5:** Examples of how altering the parameters in §4.1.3 changes the structure of the rubble pile. The bottom row shows rubble piles with large cores,  $f_c = 0.35$  and the top row shows smaller cores with  $f_c = 0.15$ . The first column is for an icy mantle with  $k_m = 0.27$ , the second shows a rockier structure with  $k_m = 0.43$  with no crust, and the third has a rocky mantle and water-rich crust,  $k_l = 0.1$  that occupies a volume fraction,  $f_l = 0.3$ . Layers are color-coded by density relative to the core and radii are to scale.

## 4.2 REBOUND and PKDGRAV Discrepancies

Despite using the same integration scheme, when replicating simulations from Veras et al. (2017) in REBOUND with the LEAPFROG integrator, there were serious discrepancies. Simulations which in Veras et al. (2017) led to mantle disruption, where the core of the rubble pile remains coherent while mantle particles are stripped stochastically at the Lagrange L1 and L2 points, were fully disrupted in REBOUND. Upon further testing, while increasing the  $\rho_b$  of rubble piles in REBOUND slowed the timescale of disruption, even extremely high densities were unable to maintain core cohesion for  $> 50$  orbits. Despite placing a higher density rubble pile ( $\rho_b = 5.5 \text{ g cm}^{-3}$ ) at the same orbital distance as the simulation from Figure 4.6, after 10 orbits the REBOUND version has occupied much more of the ring than the same epoch from Figure 4.6 (see Figure 4.7 for comparison). The core remains coherent for this rubble pile, but only for another 20 orbits, even though it should be beyond the core's Roche limit. These simulations were run using both the LEAPFROG and WHFAST integrators with similar results. After correspondence with the authors of the code, it became clear that REBOUND is not currently equipped to handle global rubble pile simulations like PKDGRAV because of the order in which the gravitational forces are calculated.

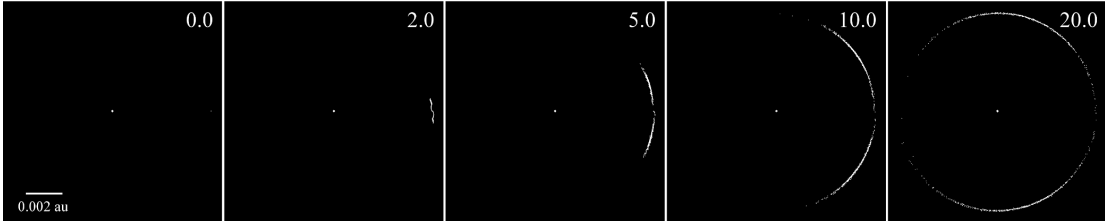


**Figure 4.6:** Figure 6 from Veras et al. (2017), showing the spread of particles from a rubble pile ( $\rho_b = 3.5 \text{ g cm}^{-3}$ ) that was only partially disrupted over multiple orbits, streaming mantle particles from the L1 and L2 Lagrange points intermittently while the core remained intact. Particle sizes are inflated to increase visibility. These simulations were done with PKDGRAV.

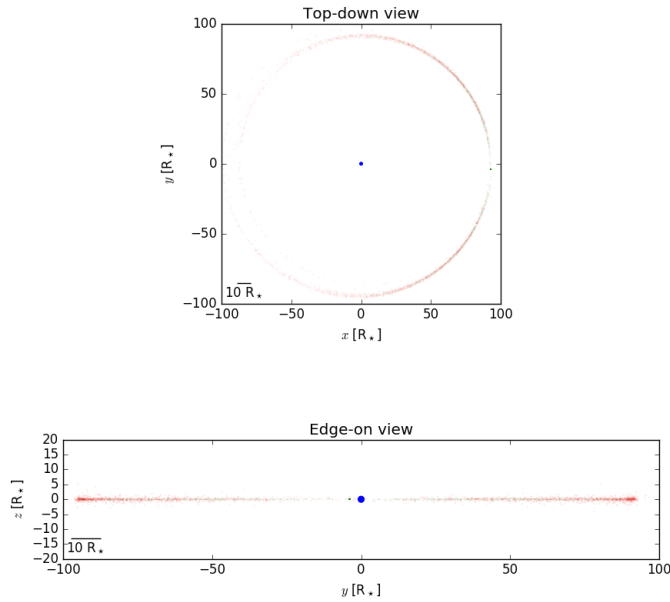


**Figure 4.7:** The white dwarf is the blue dot in the center while the red and black dots are mantle and core particles respectively. The scalebar shows  $10 R_*$ ,  $\sim 5 \times 10^{-4} \text{ AU}$  and particles have been inflated to increase visibility.

In PKDGRAV, the star is a central potential which acts on the particles **after** their accelerations due to mutual attraction have already been calculated. The star is never treated as a particle itself, unlike REBOUND. The order of solving for

the Hamiltonians in both LEAPFROG and WHFAST shift the positions of the particles on Keplerian orbits, then attempt to find the velocity shift due to interactions between particles, which does not apply to the physical scenario of a rubble pile, where individual particles' primary orbit is the rubble pile itself instead of the host star. IAS15, which directly calculates forces, fails because in its attempt to adapt the timestep to the shortest relevant dynamical timescale, changes  $dt \approx 10^{-5}$  seconds. The adjacent, well-packed rubble pile would have a number of low-impact collisions that effect little change, but IAS15 is still forced to resolve. I attempted to modify an additional force parameter in REBOUNDx to act as a central force identical to gravity, but was unsuccessful.

### 4.3 Debris Cloud Approximation

Ideally, I would either correctly implement the central force fix described above or use PKDGRAV itself to find the true photometric signature of differently structured rubble piles, but in the interest of time I used an approximation: the debris clouds of the disrupted rubble piles from REBOUND after 1 orbit. While it is not possible to conclusively state that REBOUND is showing the accelerated disruption of the rubble piles, we can still compare the timescales of disruption using the ring-filling time metric,  $t_{\text{fill}}$  from Veras et al. (2017) (see Figure 4.8).

The rubble pile is completely disrupted when its particles have formed a roughly symmetric ring around the white dwarf, with the center-of-mass at  $r = 0.0$ . The time to achieve this state is  $t_{\text{fill}}$ , and Veras et al. (2017) shows that for  $10^{19} \lesssim M_b \lesssim 10^{22}$  kg,  $10 \lesssim t_{\text{fill}} \lesssim 100$  days. For identical simulation parameters, it appears that the LEAPFROG REBOUND simulations have a shorter  $t_{\text{fill}}$  by a factor of 2 – 3.

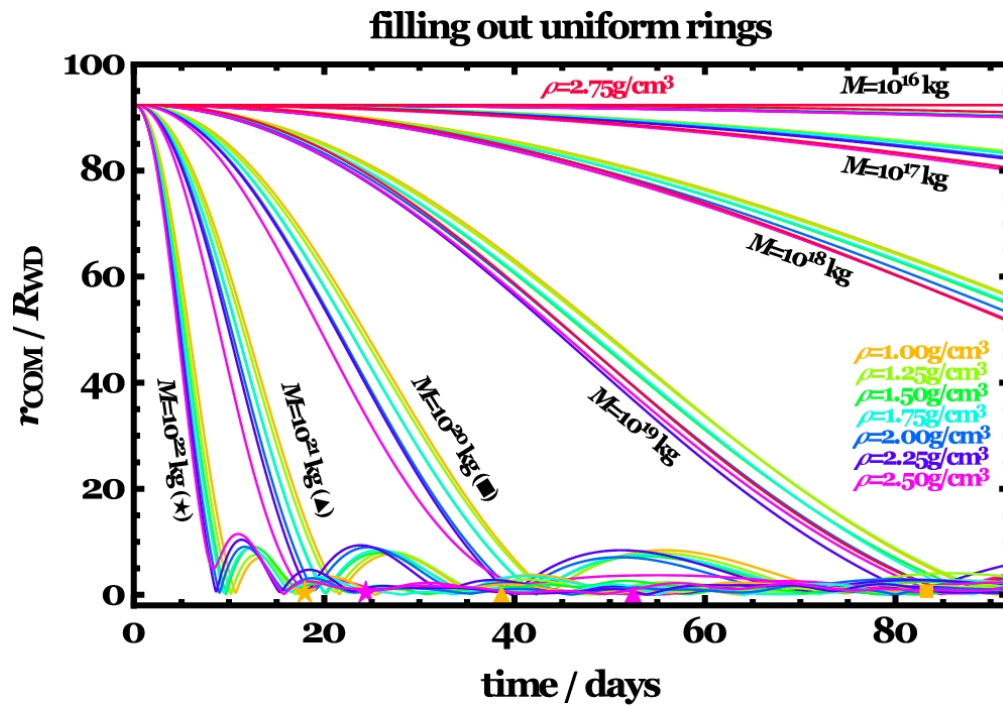


**Figure 4.8:** Figure 14 from Veras et al. (2017), showing the time it takes for homogeneous rubble piles of varying  $\rho_b$  to fully disrupt into rings. Lines with symbols indicate analytical predictions from Equations 8, 10 from Veras et al. (2017). The others are numerically determined from simulations.

### 4.3.1 Known and Inferred Properties of the Planetary Material

Based on the spectroscopic evidence, we know that the planetary material is rocky in nature, resembling Earth to first-order. However, this would also be consistent with the core of a giant planet stripped of its atmosphere or an icy planet like Neptune. Spectroscopy alone is not able to constrain the volatile content that these planetary bodies may have had (or still retain). By constructing rubble piles whose structures reflect these differences and finding the differences in the debris clouds caused by their disruption, the hope is to combine the simulations and photometry to understand the planetary interiors instead.

For certain assumptions about the equation of state governing the properties of planetary interiors, a bulk density and mass can lead to well-defined transitions between layers of the planet. Early work on the Earth in Dziewonski & Anderson (1981) led to the Preliminary Reference Earth Model (PREM). Valencia et al. (2006) created similar models for  $\frac{M_p}{M_\oplus} = 2-10$  (including PREM for  $\frac{M_p}{M_\oplus} = 1$ ), and using a different set of assumptions created Super-Mercury models for  $\frac{M_p}{M_{\text{Mercury}}} = 1-10$  (See Figures 4.9 and 4.10). For both of these, the ratio between the average core density and average lower mantle density hovered around  $\sim 0.43$ . In the Super-Earth models, a watery crust with a density ratio  $\sim 0.1$  was observed. To approximate an icy/water-rich mantle, the mean  $\sim 0.27$  was chosen. A more sophisticated treatment would use these models generated for bodies with a mass  $\leq 10^{20}$  kg instead for a variety of compositions and treat the icy mantle explicitly. The core volume fraction varied significantly across these models, 0.1 - 0.4.

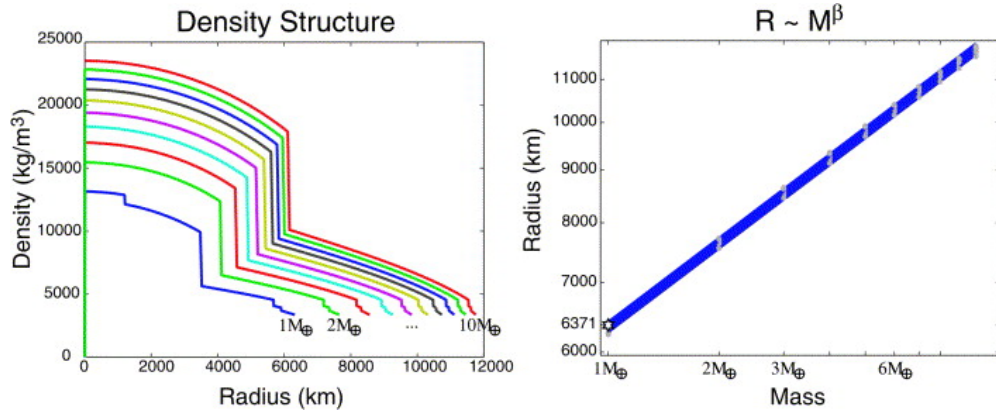


**Figure 4.9:** Density profiles for planets with Earth-like compositions and masses ranging from 1 – 10  $M_{\oplus}$

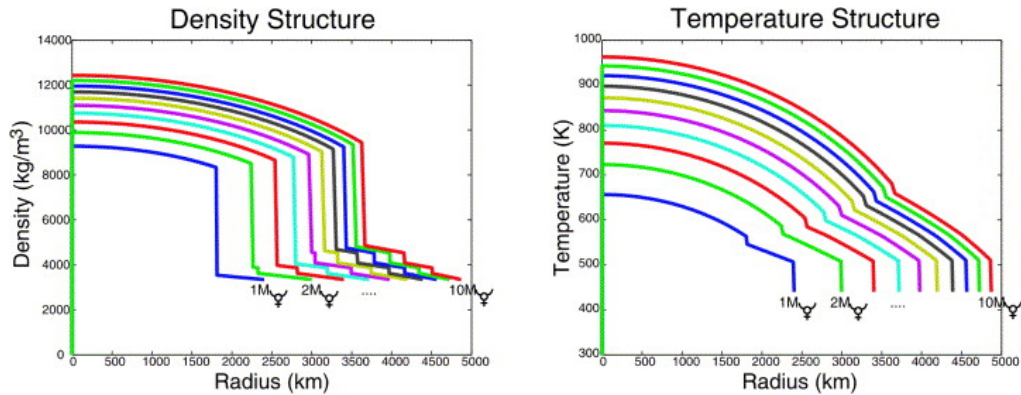


**Figure 4.10:** Density profiles for planets with Mercury-like compositions and masses ranging from 1 – 10  $M_{\text{Mercury}}$

| Template Name | $\rho_b$ [g cm <sup>-3</sup> ] | $f_c$ | $k_m$ | $f_m$ | $k_l$ | $f_l$ |
|---------------|--------------------------------|-------|-------|-------|-------|-------|
| 3_27_0_35     | 3                              | 0.35  | 0.27  | 0.65  | 0.0   | 0.0   |
| 3_27_0_15     | 3                              | 0.15  | 0.27  | 0.85  | 0.0   | 0.0   |
| 3_43_0_35     | 3                              | 0.35  | 0.43  | 0.65  | 0.0   | 0.0   |
| 3_43_0_15     | 3                              | 0.15  | 0.43  | 0.85  | 0.0   | 0.0   |
| 3_43_1_35     | 3                              | 0.35  | 0.43  | 0.35  | 0.1   | 0.3   |
| 3_43_1_15     | 3                              | 0.15  | 0.43  | 0.55  | 0.1   | 0.3   |
| 4_27_0_35     | 4                              | 0.35  | 0.27  | 0.65  | 0.0   | 0.0   |
| 4_27_0_15     | 4                              | 0.15  | 0.27  | 0.85  | 0.0   | 0.0   |
| 4_43_0_35     | 4                              | 0.35  | 0.43  | 0.65  | 0.0   | 0.0   |
| 4_43_0_15     | 4                              | 0.15  | 0.43  | 0.85  | 0.0   | 0.0   |
| 4_43_1_35     | 4                              | 0.35  | 0.43  | 0.35  | 0.1   | 0.3   |
| 4_43_1_15     | 4                              | 0.15  | 0.43  | 0.55  | 0.1   | 0.3   |

**Table 4.2:** Templates tested for debris cloud approximation, based on structures in Figure 4.5 and Table 4.1

### 4.3.2 Simulation Parameters

Given these rough assumptions, I tested permutations of:

- $\rho_b = 3$  or  $4$  g cm<sup>-3</sup>
- $f_c = 0.15$  or  $0.35$
- $k_m = 0.27$  or  $0.43$
- $f_l = 0$  or  $0.3$  (but only  $\neq 0$  if  $k_m = 0.43$ )
- $k_l = 0.1$  (only if  $f_l \neq 0$ )

The remaining parameters could be solved for when these were fixed, with a total of 12 template rubble piles, 6 per  $\rho_b$  with identical structure (the ones displayed earlier in Figure 4.5). After the debris clouds reached a fraction of  $t_{\text{fill}}$  between  $0.1 - 0.4$ , chosen such that their transit durations were  $\sim 15$  minutes, comparable to early K2 observations, I saved the simulation. Then I generated

lightcurves for each template by dividing the face of the white dwarf into 5000 pixels and counting the obscured fraction of pixels after projecting all particles in the simulation along a line-of-sight.

### 4.3.3 Savitzky-Golay Filtering

Due to the pixel-counting method, there were some small variations between consecutive timesteps that were fractional and likely an artifact of particles obscuring each other. I removed these high-frequency oscillations using the Savitzky-Golay filtering method, where low-order polynomials are fit to successive subsets of the data, creating a moving average with lower scatter than the original data without extreme distortion of the signal Savitzky & Golay (1964). After filtering, the lightcurves looked like Figure 4.11. Finally, these saved templates were interpolated as a function on the interval  $[0,1]$ , to create a lightcurve whose duration, depth, and position could be fit to individual transit signals.

### 4.3.4 Effects of Structure on Template Lightcurves

The similarities between identically structured templates of different densities can be seen by eye (Figure 4.12), but were also confirmed by calculating a  $\chi^2$  test to see which combination of templates were maximally different from each other. Expanding the list to 6 templates, 5 were from the  $\rho_b = 4 \text{ g cm}^{-3}$  group while the last was the structural equivalent of the remaining  $\rho_b = 4 \text{ g cm}^{-3}$ . For simplicity, I only used the higher density lightcurves for fitting in my analysis.

Looking at the 6 templates, where each represents a unique structure, we can see how changing individual aspects of the structure affects the lightcurve of the disrupted debris cloud. In Figure 4.13, we can see that increasing the core

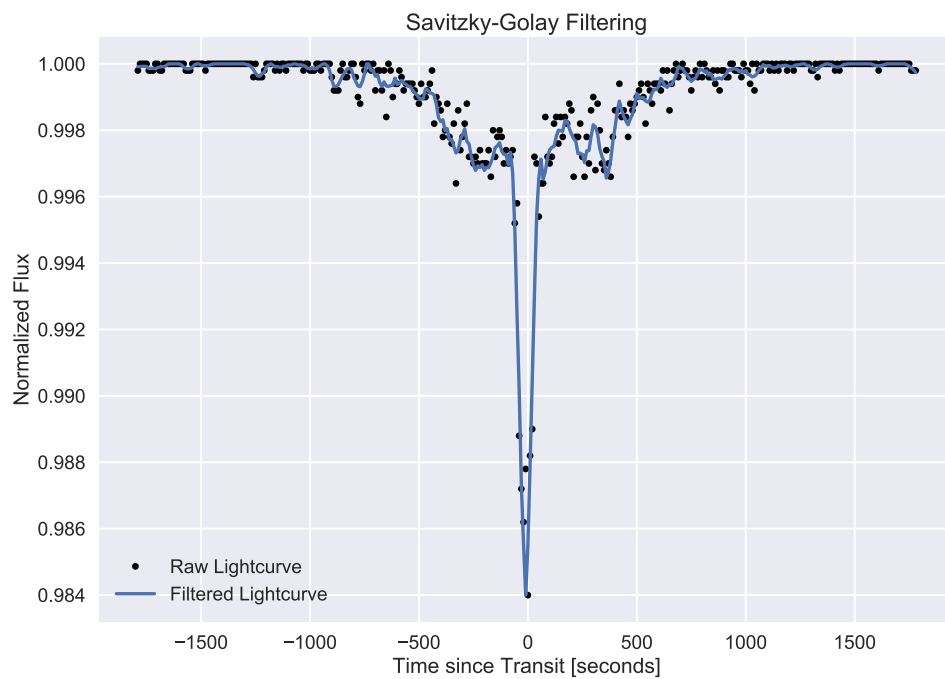


**Figure 4.11:** Raw and filtered lightcurve for Template 4\_43.0\_15. The spike is where the intact core causes the greatest obscuration while the wings are from the disrupted mantle material. The asymmetry is caused by the differences in streaming rates from L2 and L2. This structure assumes all particles are equally inflated, i.e. outgassing or sublimating identically.

| Template Name | $\rho_b$ [g cm <sup>-3</sup> ] | $f_c$ | $k_m$ | $f_m$ | $k_l$ | $f_l$ |
|---------------|--------------------------------|-------|-------|-------|-------|-------|
| 4_27_0_35     | 4                              | 0.35  | 0.27  | 0.65  | 0.0   | 0.0   |
| 4_27_0_15     | 4                              | 0.15  | 0.27  | 0.85  | 0.0   | 0.0   |
| 4_43_0_35     | 4                              | 0.35  | 0.43  | 0.65  | 0.0   | 0.0   |
| 4_43_0_15     | 4                              | 0.15  | 0.43  | 0.85  | 0.0   | 0.0   |
| 4_43_1_15     | 4                              | 0.15  | 0.43  | 0.55  | 0.1   | 0.3   |

**Table 4.3:** Templates chosen for fitting in §5.

fraction,  $f_c$ , shifts the position of the peak obscuration slightly and decreases relative strength of the wings, which is consistent with the assumption that the core causes the spike mid-transit while the wings are from the trailing mantle material; increased  $f_c$  means less material in the mantle, weakening the wings. Similarly, increasing the density of the mantle allows the rubble pile to stay more coherent and shows similarly dampened wings (see Figure 4.14) without shifting the peak. Adding the crust to the small core template however, shown in Figure 4.15, shifts the spike in the same direction while increasing the strength of the wings and the asymmetry profile of the transit curve as a whole; the crust is stripped more easily and the L1, L2 disparity becomes more apparent. But in the case of the larger core, Figure 4.16, the addition of the core is insignificantly different, so I eliminated Template 4\_43\_0\_35 from the final list (see Table 4.3).

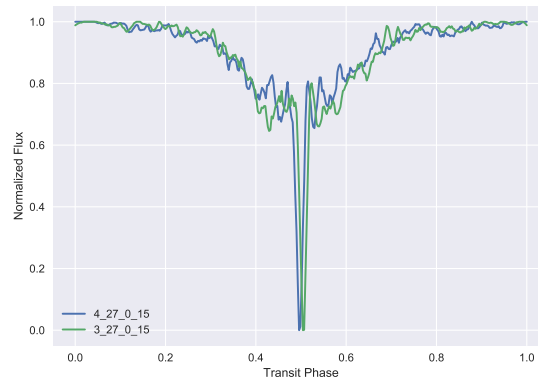


**Figure 4.12:** Rubble piles with identical structure but different densities show the least  $\chi^2$  variation.

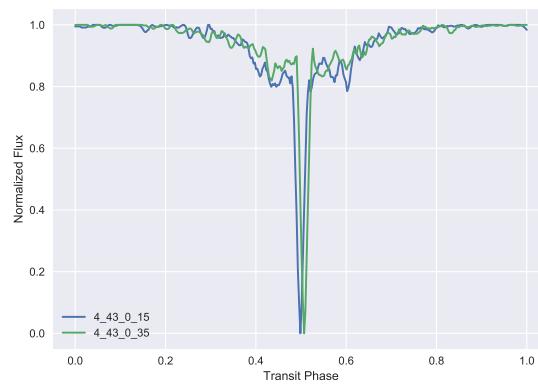


**Figure 4.13:** Increasing the core fraction  $f_c$  shifts the peak and changes the asymmetry profile.

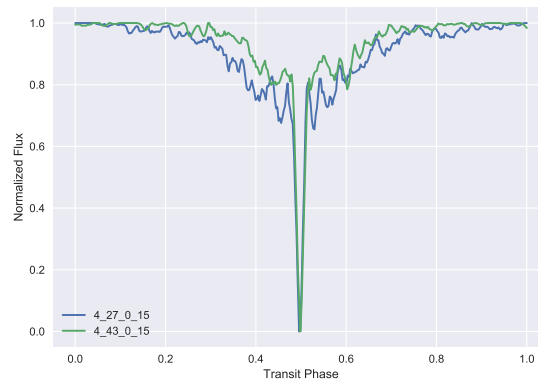


**Figure 4.14:** Increasing the mantle density slightly shifts the peak and strongly dampens the wings.

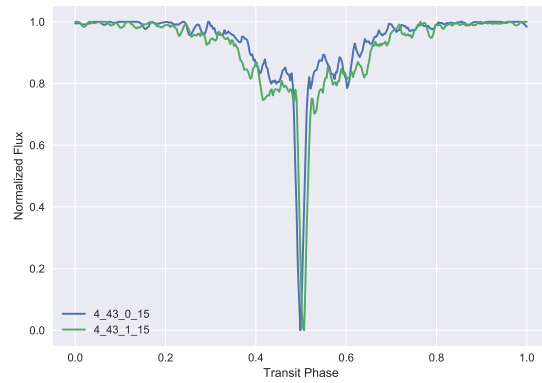


**Figure 4.15:** Adding a crust to the small core rubble pile shifts the peak and strengthens the wings.

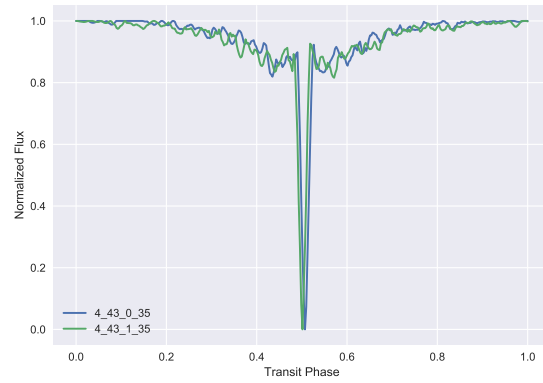


**Figure 4.16:** For the larger core, adding the crust causes no observable changes to the lightcurve.

# Chapter 5

## Photometry

WD1145+017 has shown dramatically variable photometry, with the measured periodicities of transit signals and their depths changing over the course of weeks. Even the 80-day K2 Campaign 1 lightcurves show significant changes in form (see Figure 5.1). Rappaport et al. (2016) introduced a modified waterfall plot to keep track of phase shifts and map out the changes in dip strength over the course of their ground-based monitoring campaign, a method that was adopted by later observers like Gary et al. (2017) (see Figure 5.3). Other monitoring campaigns used multiband photometry to look for wavelength dependent changes. A summary of major findings across all photometry monitoring campaigns is described in §5.1. Using the template debris cloud lightcurves from §4, I attempted to fit data taken from Hallakoun et al. (2017).

### 5.1 Summary of Features from all Datasets

The constraints we have from these papers are that:

- The initial K2 amplitudes were  $\lesssim 3\%$  of the total flux and the transits were  $\sim 1$  hour long. The most significant period was  $\sim 4.5$  hours, but other weaker signals were found at slightly longer periods with a similar phase (Vanderburg et al. 2015). K2 C1 was June - Aug 2015.
- Followup ground-based observations from the 1.2 m telescope and 0.7 m

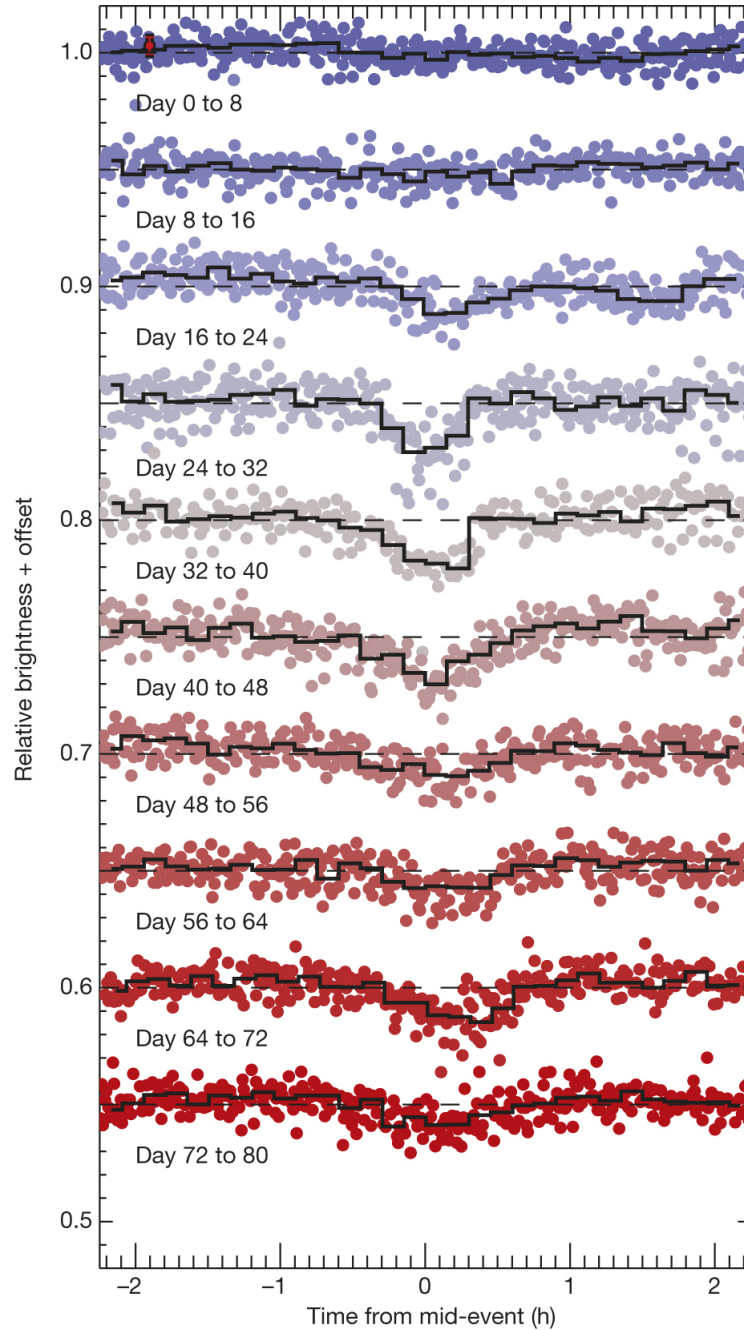


**Figure 5.1:** The initial detection in K2 Campaign 1 of transiting planetary material orbiting WD1145+017 in K2 lightcurves. Even over the  $\sim 80$  day K2 campaign, the transits showed variability in multiple aspects: the depth, asymmetry profile, and duration. Figure 2 of Vanderburg et al. (2015)

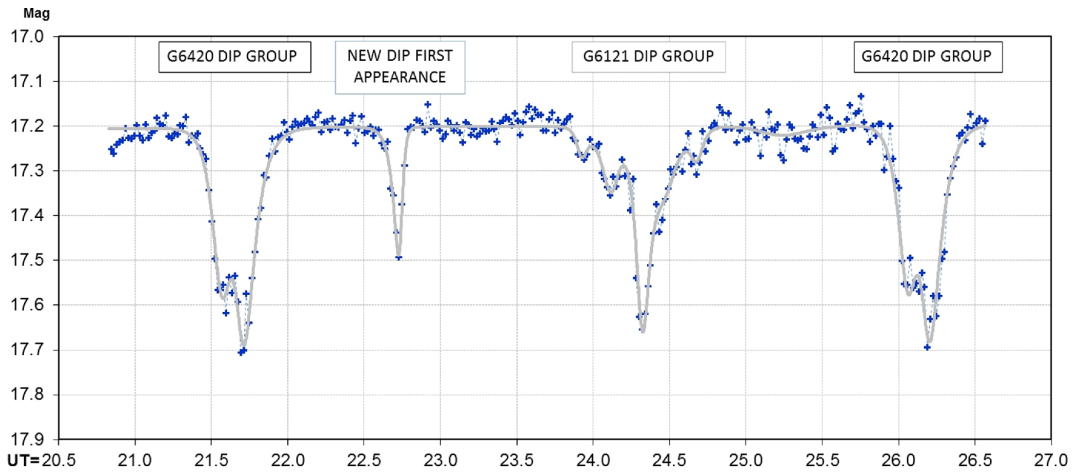


**Figure 5.2:** A single night (26 April 2016) from the monitoring campaign described in Gary et al. (2017). Specific transit signals with similar periods but different structures and phase are labelled.

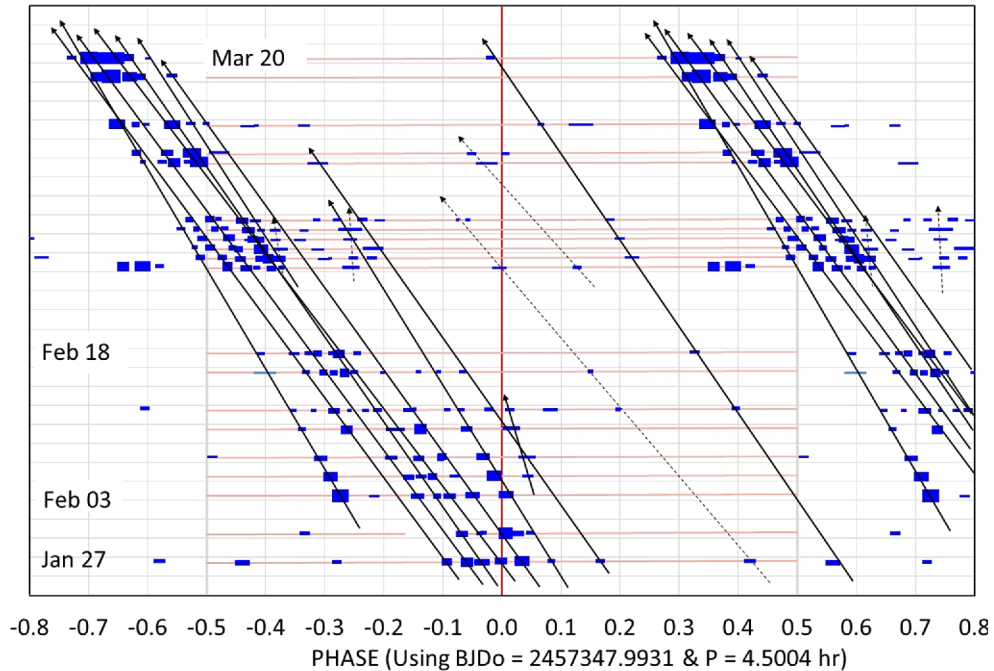


**Figure 5.3:** A waterfall plot showing the phase shifts of certain periodic signals relative to each other. The size of rectangles correspond to amplitude of dips observed and the lines are drawn to match signals thought to be related. These may be incorrect, especially in regions where different transit structures may overlap. Figure 5 from Gary et al. (2017)

MINERVA telescope at the Fred L. Whipple Observatory (Mount Hopkins, Arizona) and four 0.4 m MEarth-South Array telescopes at the Cerro Tololo Inter-American Observatory in Chile found deeper  $\sim 15\%$  transits that were  $\sim 5$  minutes long and inconsistent in phase, but all associated with a  $\sim 4.5$  hour period. These observations were taken throughout April 2015 (Vanderburg et al. 2015).

- Croll et al. (2017) used a number of telescopes throughout May 2015 in multiple bands to try to constrain the wavelength-dependence of the transit depths. Their periods, depths, and durations were roughly consistent with the ground-based photometry from Vanderburg et al. (2015). They were unable to detect any wavelength-dependence and based on the quality of data and wavelengths observed, concluded that the occulting material was composed of grains  $> 0.8 \mu\text{m}$  in size.
- Rappaport et al. (2016) identify the dominant period at 4.5004 hours and detect smaller signals that drift in phase relative to it, indicating a period of 4.4928 hours. They make use of data from multiple telescopes collected from November 2015 to January 2016.
- Gary et al. (2017) continue this monitoring campaign till July 2016 and note the sudden appearance of many transit features with an orbital period  $= 4.4912$  hours during January 2016, and later detect a new transit feature with a period corresponding to the “B” period Vanderburg et al. (2015) identified in the K2 data.
- Gänsicke et al. (2016) used the frame-camera ULTRASPEC (Dhillon et al. 2014) mounted on the 2.4 m Thai National Telescope at Doi Inthanon to find

six distinct deep ( $\sim 10 - 40\%$ ) transits with nearly identical periods between 4.491 – 4.4951 hours, but separated in phase. Smaller signals without any clear period were also found. All clearly individual transits were all 3 – 10 minutes long, but superpositions of individual features were common, creating apparent transit signals  $\sim 1.5$  hours long.

- Hallakoun et al. (2017) obtained multi-band photometry in  $u'$ ,  $g'$ ,  $r'$ ,  $i'$  using the ULTRACAM triple-beam ultra-fast camera (Dhillon et al. 2007) mounted on a 3.6 m telescope at La Silla Observatory, Chile to search for color differences like Croll et al. (2017) during April 2016. Surprisingly, they detected deeper transits in redder wavelengths than blue, which runs counter to the intuition of dusty material absorbing more blue flux. Hallakoun et al. (2017) conclude that the most likely explanation is the variability in CSA outlined in Redfield et al. (2017) and Chapter 2.

## 5.2 Fitting with Templates

Given these templates, I allow each one to be scaled in width and amplitude and shifted to match individual transit features found in the datasets available. Since all templates use the same number of free parameters, both in their original setup and in the scaling process, an F-test is not required to identify the best-fit template. Template 4.27.0.15, the icy mantle small-core rubble pile resembling Callisto, consistently provides the lowest  $\chi^2$  for all identifiable single features, though 4.43.1.15, the rocky mantle small-core rubble pile with a crust resembling Vesta, is a close second. One of the transit signals, labelled A2 in Hallakoun et al. (2017), has a much broader maximum depth than other structures or the debris clouds without resembling the classic transit light-curve. The durations

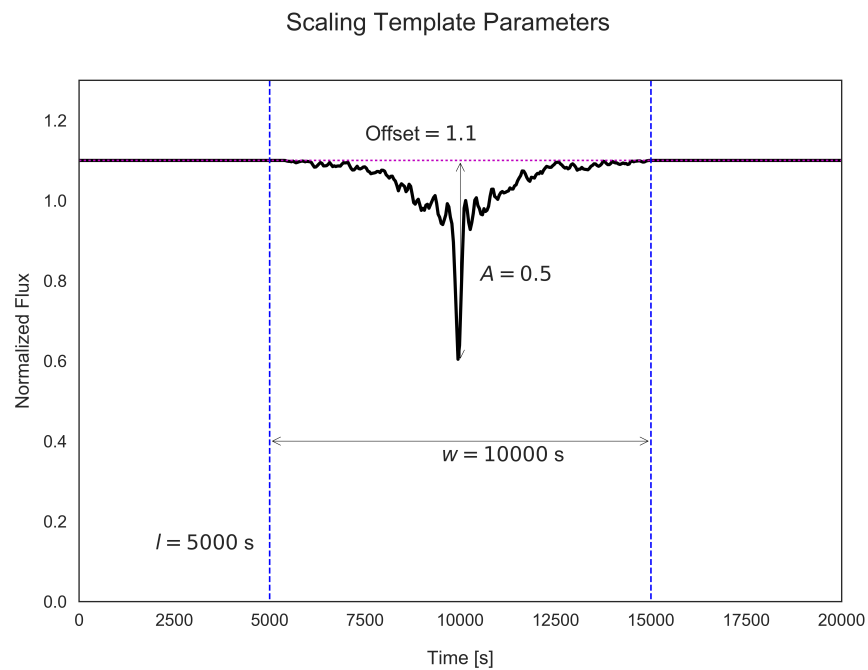


**Figure 5.4:** The templates can be scaled by stretching them in duration,  $w[s]$ , or the flux obscured,  $A$ . They can also be shifted in position, with the default unobscured flux = Offset and the starting position of the transit at  $l[s]$ . Different halves of the transit cannot be stretched relative to each other along the  $x$  or  $y$  axes, preventing the scaling model from being too flexible.

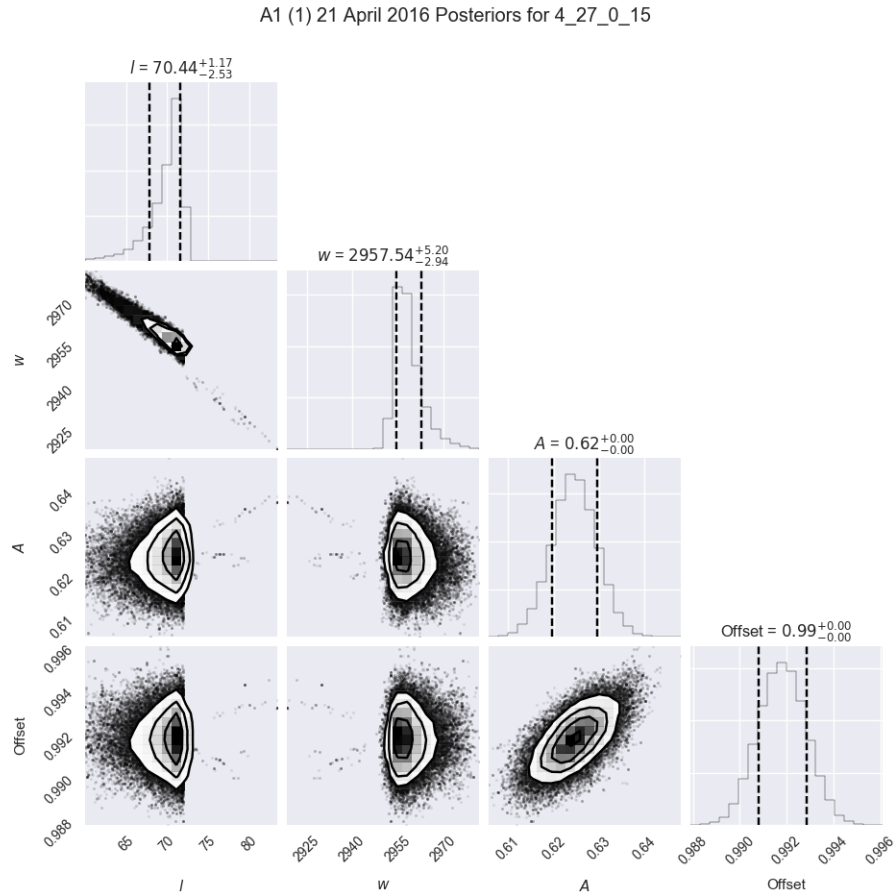


**Figure 5.5:** An example of the posterior distributions for the best-fitting template to the A1 signal from Hallakoun et al. (2017) as it appeared on 21 April 2016. The egress was contaminated by a separate transit signal, so the data was cut off early affecting the quality of the fit

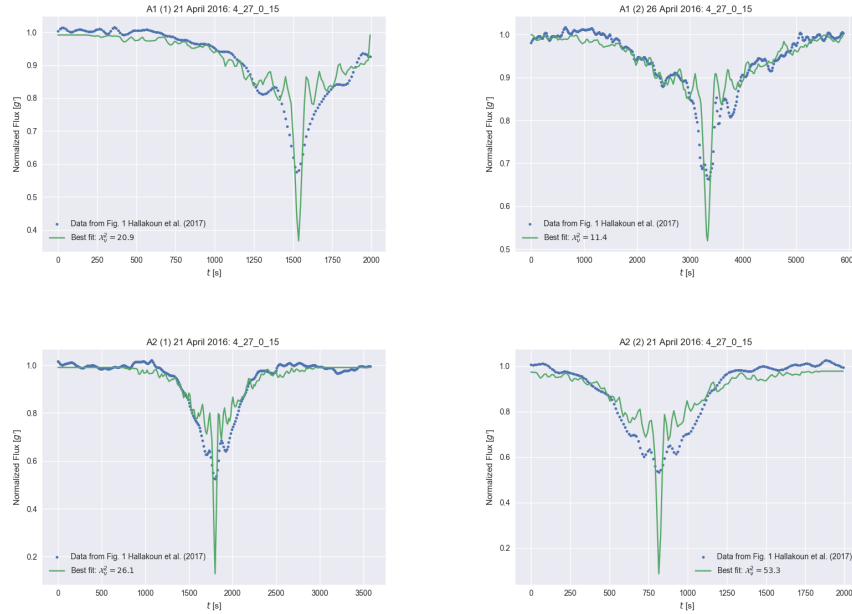


**Figure 5.6:** For all identifiable individual transits, I fit all templates using the scaling method outline in Figure 5.4, but the best fit was always Template 4\_27\_0\_15.

of transits increase over time, consistent with the debris from a single disrupted body streaming into extended tails that grow longer as the planetary material loses coherence. The template scaling can account for this by stretching in duration, but the asymmetry profile changes too much for it to remain a good fit.

To account for the large transit depths, which have increased dramatically since the original K2 transits but have stayed relatively consistent since then, we must assume that the material is projecting a large covering fraction on the face of the star. The explanation that Rappaport et al. (2016) provided was of individual fragments breaking off from a parent body, each of which expels gas and dust for a period of time before becoming “inactive”. Different compositions would sublimate and outgas different amounts given the same exposure to light from the white dwarf and collision conditions. Since the template is better fit by the small  $f_c$  and lower  $\rho_m$ , the debris cloud for those transits could have originated

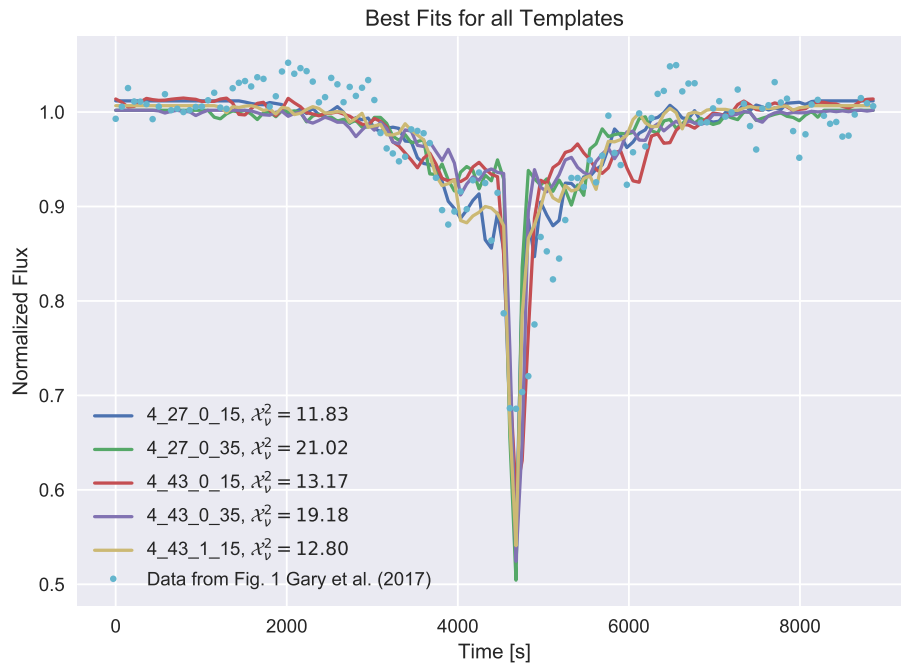


**Figure 5.7:** The best-fit scaling model for each template against the A1 feature identified in both Hallakoun et al. (2017) and Gary et al. (2017) using the Gary et al. (2017) data. Template 4\_43\_1\_15 comes close to Template 4\_27\_0\_15, but does not match the asymmetry profile quite as well.

from an icy planet or comets which formed beyond the snow line, or from a rocky planet with a water-rich mineral mantle and crust. The first two cases are unlikely because the sublimation rate would be too high to sustain the prolonged transit activity we see, but there needs to be some volatile content to explain the high transit depths and detected O I CSA.

### 5.3 “Forward Modelling”

Using the long-term simulations we used to explore stability in Chapter 3, we retrieved four epochs saved in the Simulation Archive: 1, 79, 729, and 3619 days. Integrating these forward by  $\sim 32$  hours in steps of 10 seconds, we constructed lightcurves with just the fragments and parent body using the pixel-counting method outlined in Chapter 5. Since the stability simulations indicated that the  $M_b \sim 10^{18-20}$  kg and  $e = 0$  simulations best matched the observational constraints for all attempted values of  $N_{\text{frag}}$ , I chose a simulation that satisfied those conditions.

These simple lightcurves were used to determine where the transits of individual bodies occurred and to look at their relative phase. Then we replaced the transits with scaled versions of the templates, altering their duration and amplitude to increase over time to match the constraints from §5.1. These injected lightcurves are not fits to the data, but if clear trends in  $w$  and  $A$  are found over time for more transit features, they can inform the injection process.

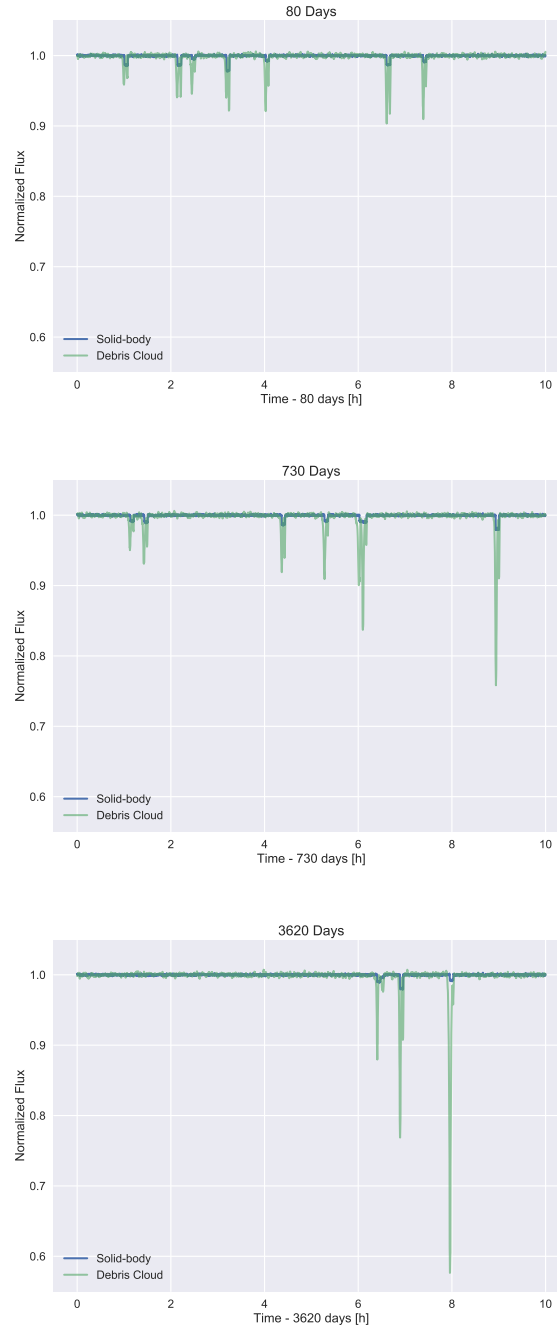


**Figure 5.8:** The blue line shows the simple lightcurve from the simulation assuming that each fragment is a solid-body (inflated by a factor of 5) while the green line replaces those solid-body transits with a random debris cloud structure. Three separate epochs are shown, each with a higher range of probable  $A$  and  $w$ . During the interval between  $t = 730$  days and  $t = 3620$  days, collisions knocked multiple fragments out of the plane, reducing the number of visible transiting bodies.

# Chapter 6

## Conclusions and Future Work

This study of the WD1145+017 system attempted to unify spectroscopic and photometric observations of the planetary material by simulating the data's possible origin. The high column densities of Fe and Ca relative to other metals, combined with the presence of O I (see §2.3), suggest that the original planetary body or bodies possessed minerals that resemble material from both the core and crust of a rocky planet. However, our modelling of the photometry indicates that the material that is outgassing and creating the observed transit signatures has a very small core fraction and low density mantle (see §4.3.4, 5.2), resembling a water-rich mineral mantle from an asteroid with a partially differentiated structure like Vesta (Veras et al. 2017).

These bodies are low mass ( $< 10^{18}$  kg, see §3.2) compared to the total accreted material inferred by accretion rates,  $\sim 10^{23}$  kg (Redfield et al. 2017) and appear to be fragmenting from a larger  $\sim 10^{19}$  kg asteroid. Each of these fragments has a bulk density high enough to avoid being immediately disrupted, but low enough that they undergo mantle disruption and maintain coherent structure for weeks (see §5.1). As these fragments disrupt, they fill out a clumpy inhomogeneous ring which leads to a continuous but irregular obscuration of flux from the white dwarf, but may also be feeding a disk closer in to the white dwarf causing variable circumstellar absorption (see §2.4).

## 6.1 Possible Formation/Destruction Scenario

To explain the majority of these results, I propose that an initially large asteroid or minor planet, roughly Ceres-sized, experienced a cataclysmic event that fragmented it at some point prior to our observations of the system, possibly during the process of stellar evolution. The remnants from this body remained in closely spaced circular orbits, with some becoming gravitational aggregates like Itokawa. These bound remnants were largely composed of mantle material from the original body and were volatile rich, and perhaps even ices (adding a weak extra bonding strength to the aggregate). Those remnants which did not become bound were eventually disrupted and/or collisionally eroded, becoming the dominant source of the accretion onto the white dwarf.

One large aggregate with  $\rho_b \sim 3\text{--}4 \text{ g cm}^{-3}$  and  $M_b \sim 10^{20} \text{ kg}$  migrated inwards to a point near its Roche limit and became the parent body; the dominant ‘A’ period detected by Vanderburg et al. (2015). Radiation and tidal forces separated fragments from this aggregate which initially stayed very close to the parent body in both phase and period, but as they drifted apart began to tidally disrupt. Since the original remnants were from a large differentiated body, they retain some core material and do not immediately undergo total disruption. As these fragments continue break off, the aggregate may become composed entirely of material too dense to be disrupted at its orbital distance or disrupt entirely. However, collisions and orbital instability may force an entirely different outcome.

## 6.2 Future Work

As photometric monitoring campaigns continue to constrain the number of fragments outgassing in the system, we should be able to predict the remaining time left for this stage of WD1145+017's planetary system life cycle. Adaptive optics imaging to study the debris disk and rule out the presence of an additional gravitational influence on the system would also help determine the conditions required for a similar post-main sequence planetary system's destruction in action. Fitting each periodic feature with debris clouds that correspond to specific structures as they evolve over time would be a computationally intensive exploration of parameter space, but a way to better test the observational signatures of differently structured rubble piles. Additionally, simulating the destruction of the original large planetary body and the subsequent formation of the gravitational aggregate would lend weight to the scenario outlined above. Both of these tests would be improved by determining the exact differences in the N-body codes `REBOUND` and `PKDGRAV` to ensure that these results are genuinely reproducible.

WD1145+017 is a singular opportunity to study post-main sequence planetary systems across multiple observational and theoretical approaches. Studying its evolution with the James Webb Space Telescope and Giant Magellan Telescope can be complemented by developments in massively-parallel computational simulations that incorporate ever more complicated physics; informed by Atacama Large Millimeter Array observations of protoplanetary and debris disks and astrochemical studies of these extreme conditions. As surveys find more systems like WD1145+017, just as the field of exoplanets has emerged and boomed over the past two decades, necroplanetology will take on the challenge of discovering and understanding the ultimate fate of planetary systems and civilizations.

# Appendix A

## REBOUND N-body Code

### A.1 Background

REBOUND is an N-body code introduced in Rein & Liu (2012) that handles collisions, multiple integrators for different physical scenarios, and can easily be modified to incorporate additional forces such as general relativity and Poynting-Robertson drag which are already implemented in the add-on package REBOUNDx. REBOUND is completely open-source, unlike PKDGRAV (the dominant N-body code for the work cited previously), and has recently included the Simulation Archive as a way to reproduce simulations bit for bit across multiple system architectures and versions of REBOUND (Rein & Tamayo 2017). It is written in C, parallelizable, and can be accessed through a Python wrapper. As a compromise between speed and convenience, I initialized all simulations in Python and saved the computationally intensive simulations to a Simulation Archive which I restored and ran natively in C.

### A.2 Integrators

Gravity acts as a continuous function, but we can only compute its effects on  $N$  interacting particles at discrete moments, leading to unavoidable errors as a function of the number of calculation steps. Different integrators make different assumptions and choices about how and when to solve the equations of motion due to gravity, so the applications and associated errors of each integrator should

be explored before making a choice for specific experiments. REBOUND’s modular structure allows the user to choose between multiple integrators within the same code architecture, so here I describe the integrators used for my work. Equations for A.2.3 and A.2.4 are adapted from the papers which introduce them, Rein & Tamayo (2015) and Rein & Spiegel (2015) respectively, mostly reproduced exactly with some occasional changing of variables to avoid repeat usage and confusion, as well as correcting a typographical error. The majority of the relevant theory is described here, but for additional depth I refer you to the papers, documentation, and code itself (Documentation at: `rebound.readthedocs.io`, Code available at: <https://github.com/hannorein/rebound/>).

### A.2.1 Drift-Kick-Drift

Most REBOUND integrators assume that all particles are in Keplerian systems, dominated by a central potential, and use the Drift-Kick-Drift scheme to split up and simplify the Hamiltonian of any particle into

$$H = H_1 + H_2, \tag{A.1}$$

where the individual parts are determined by the specific choice of integrator, though for all of the symplectic integrators  $H_1(p)$  is the larger kinetic “drift” term, a function of the canonical momenta, and  $H_2(q)$  is the smaller potential “kick” term, a function of the canonical coordinates (Rein & Tamayo 2015). All particles are integrated under the same timestep  $dt$ , in the sequence:

- (i)  $H_1$  for half a timestep  $\frac{dt}{2}$ ,
- (ii)  $H_2$  for the full timestep  $dt$ ,

(iii)  $H_2$  for the remaining  $\frac{dt}{2}$ .

As long as the timestep, supplied by the user, is a sufficiently small fraction of the shortest relevant dynamical timescale, inter-particle interactions are well described by the kick sub-step.

### A.2.2 Leapfrog Integrator

This is the simplest integrator offered by REBOUND that I used, and is functionally equivalent to the one used by PKDGRAV. With  $H_1 = H_T = \frac{\mathbf{p}^2}{2m}$ ,  $H_2 = H_U = \phi(x)$ , and starting with an initial position and velocity  $\mathbf{x}_{t_0}, \mathbf{v}_{t_0}$ :

- (i)  $\mathbf{v}_{t_0}, \mathbf{x}_{t_0} \xrightarrow[\frac{dt}{2}]{In} H_T \xrightarrow{Out} \mathbf{x}_{t_0 + \frac{dt}{2}},$
- (ii)  $\mathbf{v}_{t_0}, \mathbf{x}_{t_0 + \frac{dt}{2}} \xrightarrow[\frac{dt}{2}]{In} H_U \xrightarrow{Out} \mathbf{v}_{t_0 + dt},$
- (iii)  $\mathbf{v}_{t_0 + dt}, \mathbf{x}_{t_0 + \frac{dt}{2}} \xrightarrow[\frac{dt}{2}]{In} H_T \xrightarrow{Out} \mathbf{x}_{t_0 + \frac{dt}}.$

The sequence outlined above is a second-order stepping scheme with a cumulative energy error  $\propto dt^2$  (Rein & Liu 2012). The leapfrog integrator can be integrated backwards in time exactly, allowing us to rewind the simulation and find events that cause chaotic behavior.

### A.2.3 WHFAST

WHFAST (Rein & Tamayo 2015) is a specific implementation of the Wisdom-Holmann algorithm first introduced independently by Wisdom & Holman (1991) and Kinoshita et al. (1991). The Wisdom-Holmann algorithm was developed in a Solar System context, treating planet-planet interactions as perturbations to the

dominant Keplerian motion of planets around the Sun. First the Hamiltonian

$$H = \sum_{i=0}^{N-1} \frac{\mathbf{p}_i^2}{2m_i} - \sum_{i=0}^{N-1} \sum_{j=i+1}^{N-1} \frac{Gm_i m_j}{|\mathbf{r}_i - \mathbf{r}_j|} \quad (\text{A.2})$$

is expressed in Jacobi (**not** Jacobian) coordinates. All particles are indexed from 0 to  $N - 1$  by distance from the center of mass of the system, including the central object at  $i = 0$ . This ordering is non-unique for special cases and liable to change during long-term evolution of the system, so all particles are given unique hashes to track activity or for additional forces that act differently on individual particles.

Transforming the Cartesian Hamiltonian in Equation A.2 to Jacobi coordinates, we arrive at

$$\begin{aligned} H = & \underbrace{\sum_{i=1}^{N-1} \frac{\mathbf{p}'_i{}^2}{2m'_i} - \sum_{i=1}^{N-1} \frac{Gm'_i M_i}{|\mathbf{r}'_i|}}_{H_{\text{Kepler}}} \\ & + \underbrace{\sum_{i=2}^{N-1} \frac{Gm'_i M_i}{|\mathbf{r}'_i|} - \sum_{i=0}^{N-1} \sum_{\substack{j=i+1 \\ j \neq 1}}^{N-1} \frac{Gm_i m_j}{|\mathbf{r}_i - \mathbf{r}_j|}}_{H_{\text{Interaction}}} \\ & + \underbrace{\frac{\mathbf{p}'_0{}^2}{2m'_0}}_{H_0}. \end{aligned} \quad (\text{A.3})$$

Each term has a straightforward physical interpretation:  $H_{\text{Kepler}}$  is the sum of Keplerian Hamiltonians for each particle orbiting an imaginary body with a mass equivalent to the total mass of all particles physically interior to it, placed at the center of mass of those particles;  $H_{\text{Interaction}}$  is the sum of all inter-particle interactions; and  $H_0$  is the motion of the entire system. Keeping  $H_0$  allows the algorithm to apply in any reference frame, not just a heliocentric one. The two

terms in  $H_{\text{Interaction}}$  are in Jacobi and Cartesian coordinates respectively, and each should be evaluated separately. Note that the first term appears in  $H_{\text{Kepler}}$  (plus one element), so it need not be recomputed for each Hamiltonian.

To integrate over a single timestep  $dt$ :

- (i) Evolve system under  $H_{\text{Kepler}}, H_0$  for  $\frac{dt}{2}$ ,
- (ii) Evolve system under  $H_{\text{Interaction}}$  for  $dt$ ,
- (iii) Evolve system under  $H_{\text{Kepler}}, H_0$  for  $\frac{dt}{2}$ .

Of these Hamiltonians,  $H_0$  and  $H_{\text{Interaction}}$  are analytically solvable.  $H_0$  is motion along a line, and  $H_{\text{Interaction}}$  is a kick-step changing the velocities of particles while keeping positions constant. Putting  $H_{\text{Kepler}}$  in Jacobi coordinates converts part of the problem into a series of two-body Kepler orbits, each of which is solved numerically.

Splitting the Hamiltonian like this adds a high-frequency oscillation to the behavior of the system (in many aspects, but particularly the energy error), that eventually average out over long timescales but manifest in large changes over the short term that may obscure interesting behavior. The Wisdom-Holmann method makes use of higher order symplectic correctors that remove these perturbations. The symplectic correctors are derived using the assumption that the dominant motion due to the central body is a harmonic oscillator while the secondary interactions are perturbations which can be approximated using delta function integrals, each with their own weights evaluated at discrete nodes:

$$H = H_0 + H_1 \sum_{k=1}^n W_k h \delta_h(t - x_k h), \quad (\text{A.4})$$

where  $x_k$  are constant steps in time.

Based on the order of the integrator, there is a bounded error term associated with any symplectic method which can be calculated and removed, though at higher orders the computational cost of calculating this error outweighs the value of the accuracy achieved. For a corrector of order  $k$ , the order (a measure of accuracy) of the integrator is  $\mathcal{O}(\epsilon dt^K) + \mathcal{O}(\epsilon^2 dt^2)$ . Without correctors, WHFAST is a second order scheme with  $\mathcal{O}(\epsilon^2 dt^2)$ , but by default implements an 11<sup>th</sup> order corrector with the option to switch to a 3<sup>rd</sup>, 5<sup>th</sup>, or 7<sup>th</sup> order corrector instead (or opt out of correctors entirely).

#### A.2.4 IAS15

Preserving the phase-space invariance and error minimization traits while hanging the timestep under symplectic integrators is difficult, though some symplectic integrators attempt to do so. Additionally, Hamiltonian methods only work when the system only has conservative forces described by a potential dependent on position. Radiation forces, which depend on the particle’s velocity, do not satisfy this condition and including them would lead to unphysical results. REBOUND includes the Implicit integrator with Adaptive timestepping, 15<sup>th</sup> order (IAS15) first described in Rein & Spiegel (2015), to deal with problems where adaptive timesteps and non-conservative forces are relevant.

Given a combination of forces we can define a function,  $\mathbf{F}[y, y', t]$  which depends on the position and velocity of a particle and returns the acceleration  $y''$  at a time  $t$ . Expanding to a seventh-order truncated series, we can approximate this as

$$y''[t] \approx y''_0 + \sum_{k=1}^7 a_k t^k \quad (\text{A.5})$$

where  $y''_0$  is the initial acceleration. Reparameterizing this series with the timestep

$dt$  and defining  $h \equiv \frac{t}{dt}$  and  $b_k = a_k dt^{k+1}$  we get

$$y''[h] \approx y''_0 + \sum_{k=1}^7 b_k h^k. \quad (\text{A.6})$$

Integrating this equation once gives us the velocity,

$$y'[h] \approx y'_0 + h dt \left( y''_0 + \frac{h}{2} \left( b_1 + \frac{2h}{3} (b_2 + \dots) \right) \right) \quad (\text{A.7})$$

and integrating again gives us position,

$$y[h] \approx y_0 + y'_0 h dt + \frac{h^2 dt^2}{2} \left( y''_0 + \frac{h}{3} \left( b_1 + \frac{h}{2} (b_2 + \dots) \right) \right). \quad (\text{A.8})$$

Dividing a single step  $dt$  into substeps and introducing two sets of constants  $g_k$  and  $h_k$ , we express equation A.6 as

$$y''[h] \approx y''_0 + g_1 h + g_2 h(h - h_1) + g_3 h(h - h_1)(h - h_2) + \dots + g_7 h \prod_{j=1}^7 (h - h_j), \quad (\text{A.9})$$

where  $h_k$  are non-equidistant spacings in the interval of  $[0,1]$ . The specific values of  $h_k$  are chosen according to Gauss-Radau spacing, which sets  $n$  nodes in the interval  $[0,1]$  to closely evaluate polynomials of degree  $2n - 1$  (related to Gaussian quadrature which evaluates polynomial integrals perfectly over the interval) while fixing one of the nodes to be either endpoint of the interval. With  $k = 7$  and the initial condition at  $h = 0$ , there are 8 nodes, making IAS15 a 15<sup>th</sup> order scheme.

Breaking down the procedure of the first timestep, given the initial position, velocity, and acceleration of a particle:

1. For each substep  $h = h_k$ , evaluate  $y[h_k]$ ,  $y'[h_k]$  using A.8 and A.7 by assuming  $b_k = 0$  for all  $k$  (acceleration is constant over the timestep)

2. Using the predicted interval positions and velocities as inputs to the forces acting on the particle (gravity and any additional defined forces), find the accelerations the particle would experience at each substep.
3. With these accelerations, solve for  $g_k$  and then rearrange to find new values for  $b_k$ .
4. Repeat the previous steps with the new  $b_k$  values for a specific number of iterations (exact conditions described below).
5. Save the  $b_k$  values after all iterations are complete to inform the starting values for the next timestep.

To determine whether  $b_k$  values are satisfactory, `IAS15` uses a convergence condition and a forced maximum of 12 iterations if the condition is not satisfied. Failing to converge after so many attempts indicates that the initial choice of timestep is too long compared to the dynamical timescale of the problem, which is easily corrected if the adaptive timestepping is enabled.

The convergence condition relates the initial acceleration  $y_0''$  to the highest order coefficient  $b_7$ . When the ratio between  $\delta b_7$ , the change in  $b_7$  over consecutive iterations, and  $y_0''$  is within machine-precision ( $\frac{\delta b_7}{y_0''} < 10^{-16}$ ) or oscillates about a mean value with no improvement, the predictor-loop converges. The mechanism for controlling the timestep is similar to the convergence criterion, but uses the absolute value of  $b_7$  instead of the change as its metric instead.

### A.2.5 HERMES

Lastly, `REBOUND` includes the `HERMES` hybrid integrator, which uses `WHFAST` over long timescales but switches to `IAS15` when particles have close encounters,

---

using a shorter timestep to resolve the secular interaction or possible collision. The close encounter is determined by measuring particle separation in Hill radii every timestep; if one particle is within 3 Hill radii of another, the integration for that timestep by `WHFAST` is ignored and `IAS15` takes over. Once the separation is sufficiently large, `WHFAST` returns with the same timestep. `IAS15` is extremely accurate, but computationally expensive, making the relative speed of `WHFAST` valuable for simulations longer than  $10^6$  orbits. However, in compact systems the frequent interactions and crossing of orbits can lead to unstable behavior for `WHFAST` because the underlying assumptions about the dominant Kepler potential are violated. This problem carries over to `HERMES` whenever it uses `WHFAST` as seen in Figure 3.1.

# Bibliography

- Agol, E. 2011, *ApJ*, 731, L31
- Baranau, V., & Tallarek, U. 2014, *Soft Matter*, 10, 3826
- Beitz, E., Blum, J., Parisi, M. G., & Trigo-Rodriguez, J. 2016, *ApJ*, 824, 12
- Borucki, W. J., Koch, D., Basri, G., et al. 2010, *Science*, 327, 977
- Brouwer, D. 1937, *AJ*, 46, 149
- Butler, R. P., Wright, J. T., Marcy, G. W., et al. 2006, *ApJ*, 646, 505
- Croll, B., Dalba, P. A., Vanderburg, A., et al. 2017, *ApJ*, 836, 82
- Deckers, J., Teiser, J., & Wurm, G. 2015, in *AAS/Division for Planetary Sciences Meeting Abstracts, Vol. 47, AAS/Division for Planetary Sciences Meeting Abstracts*, 302.02
- Dhillon, V. S., Marsh, T. R., Stevenson, M. J., et al. 2007, *MNRAS*, 378, 825
- Dhillon, V. S., Marsh, T. R., Atkinson, D. C., et al. 2014, *MNRAS*, 444, 4009
- Donev, A., Torquato, S., Stillinger, F. H., & Connelly, R. 2004, *Journal of applied physics*, 95, 989
- Draine, B. T. 2011, *Physics of the Interstellar and Intergalactic Medium* (Princeton University Press)
- Dziewonski, A. M., & Anderson, D. L. 1981, *Physics of the Earth and Planetary Interiors*, 25, 297

- Everhart, E. 1985, in Dynamics of Comets: Their Origin and Evolution, Proceedings of IAU Colloq. 83, held in Rome, Italy, June 11-15, 1984. Edited by Andrea Carusi and Giovanni B. Valsecchi. Dordrecht: Reidel, Astrophysics and Space Science Library. Volume 115, 1985, p.185, ed. A. Carusi & G. B. Valsecchi, 185
- Farihi, J. 2016, *New Astronomy Review*, 71, 9
- Foreman-Mackey, D., Hogg, D. W., Lang, D., & Goodman, J. 2013, *PASP*, 125, 306
- Fujiwara, A., Kawaguchi, J., Yeomans, D. K., et al. 2006, *Science*, 312, 1330
- Gänsicke, B. T., Aungwerojwit, A., Marsh, T. R., et al. 2016, *ApJ*, 818, L7
- Gary, B. L., Rappaport, S., Kaye, T. G., Alonso, R., & Hambschs, F.-J. 2017, *MNRAS*, 465, 3267
- Goodman, J., & Weare, J. 2010, *Comm. App. Math. Comp. Sci.*, 55, 65
- Gurri, P., Veras, D., & Gänsicke, B. T. 2017, *MNRAS*, 464, 321
- Hales, T., Adams, M., Bauer, G., et al. 2015, *ArXiv e-prints*, arXiv:1501.02155
- Hallakoun, N., Xu, S., Maoz, D., et al. 2017, *ArXiv e-prints*, arXiv:1702.05483
- Howell, S. B., Sobeck, C., Haas, M., et al. 2014, *PASP*, 126, 398
- Jura, M., Farihi, J., & Zuckerman, B. 2007, *ApJ*, 663, 1285
- Kilic, M., & Redfield, S. 2007, *ApJ*, 660, 641
- Kinoshita, H., Yoshida, H., & Nakai, H. 1991, *Celestial Mechanics and Dynamical Astronomy*, 50, 59

- Koester, D. 2009, *A & A*, 498, 517
- Koester, D., Gänsicke, B. T., & Farihi, J. 2014, *A & A*, 566, A34
- Koester, D., Girven, J., Gaensicke, B., & Dufour, P. 2010, in *American Institute of Physics Conference Series*, Vol. 1273, *American Institute of Physics Conference Series*, ed. K. Werner & T. Rauch, 492–495
- Koester, D., & Kepler, S. O. 2015, *A & A*, 583, A86
- Kreidberg, L. 2015, *PASP*, 127, 1161
- Kurucz, R., & Bell, B. 1995, *Atomic Line Data* (R.L. Kurucz and B. Bell) Kurucz CD-ROM No. 23. Cambridge, Mass.: Smithsonian Astrophysical Observatory, 1995., 23
- Leinhardt, Z. M., Ogilvie, G. I., Latter, H. N., & Kokubo, E. 2012, *MNRAS*, 424, 1419
- Loeb, A., & Maoz, D. 2013, *MNRAS*, 432, L11
- Mandel, K., & Agol, E. 2002, *ApJ*, 580, L171
- Manser, C. J., Gaensicke, B. T., Koester, D., Marsh, T. R., & Southworth, J. 2016, *ArXiv e-prints*, arXiv:1607.06810
- Mayor, M., & Queloz, D. 1995, *Nature*, 378, 355
- Michel, P., & Richardson, D. C. 2013, *A & A*, 554, L1
- Mikkola, S. 1997, *Celestial Mechanics and Dynamical Astronomy*, 67, 145
- Mociski, J., Bargie, M., Rycerz, Z. A., & Jacobs, P. W. M. 1989, *Molecular Simulation*, 3, 201

- Oke, J. B. 1990, *AJ*, 99, 1621
- Pedregosa, F., Varoquaux, G., Gramfort, A., et al. 2012, ArXiv e-prints, arXiv:1201.0490
- Rappaport, S., Gary, B. L., Kaye, T., et al. 2016, *MNRAS*, 458, 3904
- Redfield, S., Farihi, J., Cauley, P. W., et al. 2017, *ApJ*, 839, 42
- Rein, H., & Liu, S.-F. 2012, *A & A*, 537, A128
- Rein, H., & Spiegel, D. S. 2015, *MNRAS*, 446, 1424
- Rein, H., & Tamayo, D. 2015, *MNRAS*, 452, 376
- . 2017, *MNRAS*, arXiv:1701.07423
- Richardson, D. C., Michel, P., Walsh, K. J., & Flynn, K. W. 2009, *Planet. Space Sci.*, 57, 183
- Savitzky, A., & Golay, M. J. E. 1964, *Analytical Chemistry*, 36, 1627
- Seager, S., & Sasselov, D. D. 1998, *ApJ*, 502, L157
- Steinhaus, H. 1999, *Mathematical Snapshots*, Dover Recreational Math Series (Dover Publications)
- Stumpff, K. 1962, *Himmelsmechanik. Band I* (Berlin: VEB Deutscher Verlag der Wissenschaften, 1965)
- Valencia, D., O’Connell, R. J., & Sasselov, D. 2006, *Icarus*, 181, 545
- Vanderburg, A., & Johnson, J. A. 2014, *PASP*, 126, 948
- Vanderburg, A., Johnson, J. A., Rappaport, S., et al. 2015, *Nature*, 526, 546

- Veras, D. 2016a, *Royal Society Open Science*, 3, 150571
- . 2016b, *Royal Society Open Science*, 3, 150571
- Veras, D., Carter, P. J., Leinhardt, Z. M., & Gänsicke, B. T. 2017, *MNRAS*, 465, 1008
- Veras, D., Leinhardt, Z. M., Bonsor, A., & Gänsicke, B. T. 2014, *MNRAS*, 445, 2244
- Vernet, J., Dekker, H., D’Odorico, S., et al. 2011, *A & A*, 536, A105
- Vogt, S. S., Allen, S. L., Bigelow, B. C., et al. 1994, in *Proc. SPIE*, Vol. 2198, *Instrumentation in Astronomy VIII*, ed. D. L. Crawford & E. R. Craine, 362
- Wisdom, J., & Holman, M. 1991, *AJ*, 102, 1528
- Wolszczan, A., & Frail, D. A. 1992, *Nature*, 355, 145
- Xu, S., Jura, M., Dufour, P., & Zuckerman, B. 2016, *ApJ*, 816, L22